

České vysoké učení technické v Praze
Fakulta jaderná a fyzikálně inženýrská

Czech Technical University in Prague
Faculty of Nuclear Sciences and Physical Engineering

Doc.Ing. Richard Liska, CSc.

**Numerické metody pro modelování stlačitelného
nevazkého proudění laserového plazmatu**

**Numerical methods for modeling of compressible
inviscid flow of laser plasma**

Summary

Compressible inviscid fluid flow is described by Euler equations expressing conservation of mass, momentum and energy. Euler equations are presented in Eulerian formulation in the fixed coordinate frame and in Lagrangian formulation in the coordinate frame moving with the fluid. The direct and indirect Arbitrary Lagrangian Eulerian (ALE) methods are shortly introduced and the full model for laser plasma is presented. Composite schemes, consisting in global composition of several steps of the Lax-Wendroff (LW) type dispersive scheme with one step of diffusive Lax-Friedrichs type scheme, are introduced in 1D and 2D. Direct generalization of 2D LW type scheme to 3D leads to unconditionally unstable scheme. Modification of this scheme gives a sub-optimally stable scheme. Optimally stable 3D LW type unsplit scheme is derived from the fully symmetric dimensionally split scheme.

The PALE (Prague ALE) code has been developed for simulations of laser interaction with targets. It employs the indirect ALE hydrodynamical method, which computes for some time in Lagrangian formulation and then smooths the Lagrangian mesh moving with the fluid and conservatively interpolates (remaps) the conservative quantities from the Lagrangian mesh to the smoothed one. The hydrodynamics is supplemented by heat conductivity and laser absorption processes, which are necessary for laser plasma modeling. All numerical methods employed in the PALE code are summarized with remapping being covered in more detail. Flux corrected remapping, based on the idea of flux corrected transport (FCT), is developed for density. Synchronized flux corrected remapping of density, momentum and energy is presented.

Selected simulations of laser interactions with targets, including the oblique incidence of laser on a thin foil, the disc flyer target, the foam target and the massive target irradiated by an annular laser beam, demonstrate the capabilities of the PALE code. Simulations confirm the necessity to use the computational mesh moving with the plasma wherever possible and to apply indirect ALE method when the mesh becomes too distorted. Simulations correspond to experiments performed at PALS laser facility and simulations results are compared with experimental ones.

Souhrn

Stlačitelné neviské proudění tekutin je popsáno Eulerovými rovnicemi vyjadřujícími zachování hmoty, hybnosti a energie. Eulerovy jsou uvedeny v eulerovské formulaci v pevné souřadné soustavě a v lagrangeovské formulaci v souřadné soustavě pohybující se s tekutinou. Krátce jsou představeny přímá a nepřímá ALE (Arbitrary Lagrangian Eulerian) metoda a je prezentován úplný model pro laserové plazma. Složená schemata, skládající se z globálního složení několika kroků disperzního schematu Laxova-Wendroffova (LW) typu s jedním krokem difuzního schematu typu Laxe-Friedrichse, jsou představena v 1D a 2D. Přímé zobecnění 2D schematu LW typu do 3D vede k bezpodmínečně nestabilnímu schematu. Modifikace tohoto schematu dává suboptimálně stabilní schema. Optimálně stabilní 3D schema LW typu bez rozkladu je odvozeno z plně symetrického schematu dimenzionálního rozkladu.

Kód PALE (Pražské ALE) byl vyvinut pro simulace interakce laseru s terčíky. Kód používá nepřímou ALE hydrodynamickou metodu, která nějaký čas počítá v lagrangeovské formulaci a potom vyhledá lagrangeovskou síťku pohybující se spolu s tekutinou a konzervativně interpoluje (remapuje) konzervativní veličiny z lagrangeovské sítě na vyhazenou síť. Hydrodynamika je doplněna procesy tepelné vodivosti a absorpce laseru, které jsou nezbytné pro modelování laserového plazmatu. Všechny numerické metody použité v kódu PALE jsou shrnuty a remapování je probráno detailněji. Remapování korekcí toků, založené na myšlence FCT (Flux Corrected Transport), je odvozeno pro hustotu. Je prezentováno synchronní remapování korekcí toků pro hustotu, hybnost a energii.

Vybrané simulace interakce laseru s terčíky, zahrnující šikmý dopad laseru na tenkou fólii, terčík s letícím diskem, pěnový terčík a masivní terčík ozářený prstencovým laserovým svazkem, demonstrují schopnosti kódu PALE. Simulace potvrzují nezbytnost použít výpočetní síťku pohybující se spolu s plazmatem, kdekoli je to možné, a nasadit nepřímou ALE metodu když se síťka stane příliš deformovanou. Simulace korespondují s experimenty prováděnými na laserovém zařízení PALS a výsledky simulací jsou porovnány s experimentálními výsledky.

Klíčová slova: Eulerovy rovnice, diferenční schemata, analýza stability, lagrangeovské metody, ALE metody, remapování, laserové plasma, interakce laseru s terčíky

Keywords: Euler equations, difference schemes, stability analysis, Lagrangian methods, ALE methods, remapping, laser plasma, laser interaction with targets

České vysoké učení technické v Praze

Název: Numerické metody pro modelování stlačitelného nevazkého proudění laserového plazmatu

Autor: Richard Liska

Počet stran: 35

Náklad:

© Richard Liska, 2013
ISBN

Contents

1	Introduction	6
2	Euler equations for compressible fluid flow	6
2.1	Eulerian formulation	6
2.2	Lagrangian formulation	7
2.3	Arbitrary Lagrangian Eulerian (ALE) methods	7
2.4	Model for laser plasma	8
3	Numerical methods	8
3.1	Composite schemes for Euler formulation	8
3.1.1	1D schemes	8
3.1.2	2D schemes	10
3.1.3	3D schemes	11
3.1.4	Optimally stable 3D schemes based on dimensional splitting	14
3.2	Indirect ALE method	16
3.2.1	Lagrangian methods	16
3.2.2	Lagrangian mesh rezoning	17
3.2.3	Remapping	18
3.2.4	Flux corrected remapping of density	19
3.2.5	Synchronized flux corrected remapping of density, momentum and energy	22
3.3	Heat conductivity	23
3.4	Laser absorption	24
4	Simulations of laser interaction with targets	25
4.1	Oblique incidence on thin foil	25
4.2	Disc flyer target	26
4.3	Foam target	28
4.4	Massive target irradiated by annular laser beam	29
5	Outlook of the research and education in the given field	30
	References	30
	Curriculum vitae	35

1 Introduction

The compressible, inviscid fluid flow is modeled by Euler equations, which are non-linear conservation laws for mass, momentum and energy. The first two of these equations for conservation of mass and momentum were written down by Leonhard Euler in 1757 and Pierre Hugoniot added the conservation law for energy in 1889. These equations are directly solvable only in a few special cases and numerical methods have to be used to treat them.

The domain of numerical methods for compressible, inviscid fluid flow, called computational gas dynamics, forms an important part of the wider computational fluid dynamics, including also viscous and incompressible fluid flows. As the Euler equations are non-linear hyperbolic conservation laws, their solution can have discontinuities in form of shock or contact waves and the numerical methods solving them has to be designed in a special way to be able to resolve the discontinuities well. The numerical methods have to ensure that on the shock waves the kinetic energy is dissipated into the internal energy in agreement with the second law of thermodynamics. The dissipation in numerical methods is achieved either explicitly through the artificial viscosity or implicitly e.g. through approximate Riemann solvers. The conservativity of a numerical method usually guarantees the correct resolution of shock wave speed, which is one of the most important features of the conservation laws and which has to obey Rankin-Hugoniot condition.

From numerous applications of compressible, inviscid fluid flows, as e.g. in meteorology, aerospace engineering or astrophysics, we are interested in their usage for simulations of laser plasma, forming the base for Inertial Confinement Fusion (ICF). The ICF basic strategy, to achieve the controlled fusion reaction as a new source of energy, is to use high power lasers to compress and heat a small amount of the fusion fuel to conditions at which the fusion can be ignited.

Problems being simulated in laser plasma typically involve areas of compression and expansion with computational domain changing with time. Such problems are treated better by Lagrangian method with computational mesh moving together with the simulated fluid. For some types of fluid flow, as e.g. shear or vortex flows, the Lagrangian methods suffer from a serious computational mesh distortion, which can lead to inverted computational cells and consequently to the failure of the method. This problem can be overcome by using the indirect ALE method [12], which smooths the distorted Lagrangian mesh and conservatively interpolates the conservative quantities from the Lagrangian mesh to the smoothed one.

2 Euler equations for compressible fluid flow

Euler equations for compressible inviscid fluid flow express the conservation of mass, momentum and energy. There are several form of Euler equations depending on the choice of coordinates.

2.1 Eulerian formulation

Eulerian formulation assumes static, non-moving coordinate system. The conservation of mass, momentum and energy is written as

$$U_t + f(U)_x + g(U)_y + h(U)_z = 0, \quad (1)$$

where the subscripts denote partial derivatives and

$$U = \begin{pmatrix} \rho \\ \rho u \\ \rho v \\ \rho w \\ \rho e \end{pmatrix}, \quad f = \begin{pmatrix} \rho u \\ \rho u^2 + p \\ \rho uv \\ \rho uw \\ u(\rho e + p) \end{pmatrix}, \quad g = \begin{pmatrix} \rho v \\ \rho v^2 + p \\ \rho vw \\ \rho vw \\ v(\rho e + p) \end{pmatrix}, \quad h = \begin{pmatrix} \rho w \\ \rho w^2 + p \\ \rho vw \\ \rho w^2 + p \\ w(\rho e + p) \end{pmatrix},$$

and where ρ is the density, u, v, w are the components of the fluid velocity in the x, y, z -directions, $e = \varepsilon + 1/2(u^2 + v^2 + w^2)$ is the specific total energy (i.e. the total energy per unit of mass), ε is the specific internal energy and p is the pressure. The system is closed by the equation of state $p = p(\rho, \varepsilon)$. For the ideal gas it reads $p = (\gamma - 1)\rho\varepsilon$, where γ is the adiabatic exponent, defined as the ratio of specific heats. For laser plasma one can use the quotidian equation of state QEOS [41].

2.2 Lagrangian formulation

Lagrangian formulation of the Euler equations assumes coordinate frame moving together with the fluid. The Euler equations written in Lagrangian coordinates are

$$\rho \frac{dU}{dt} + \text{div } \mathbf{f}(U) = 0, \quad (2)$$

where $d/dt = \partial/\partial t + \mathbf{u} \cdot \text{grad}$ with $\mathbf{u} = (u, v, w)$ is the total Lagrangian time derivative including convective terms and

$$U = \begin{pmatrix} \eta \\ \mathbf{u} \\ e \end{pmatrix}, \quad \mathbf{f} = \begin{pmatrix} \mathbf{u} \\ -pI \\ -p\mathbf{u} \end{pmatrix},$$

and where $\eta = 1/\rho$ is the specific volume and I is the unit matrix. The movement of Lagrangian coordinates is controlled by the ordinary differential equation $d\mathbf{x}/dt = \mathbf{u}$ which after discretization describes the movement of the computational mesh. As the computational mesh is moving with the fluid, the mass of each computational cell remains constant. Lagrangian formulation suits very well for problems involving large scale changes of computational domain (changes in volume or shape) and for problems with moving boundaries (including moving boundary conditions).

For some types of flow, as e.g. shear or vortex flows, one cannot use Lagrangian formulation for sufficiently long time, as Lagrangian moving mesh after some time becomes distorted or even tangled. Such types of flow can however be treated by the Arbitrary Lagrangian Eulerian (ALE) method, introduced shortly in the next section.

2.3 Arbitrary Lagrangian Eulerian (ALE) methods

There are two versions of the ALE method. The first one, so called direct ALE method, assumes that the computational mesh movement is given (i.e. movement of each node of the mesh is given) and computes the solution on this moving mesh. The second one, so called indirect ALE method, first computes on the Lagrangian moving mesh, then either after several Lagrangian steps or when the moving mesh becomes distorted (quality of the mesh deteriorate) the rezone and remap stages are invoked. The rezone stage smooths or untangles the distorted Lagrangian mesh. The remap stage performs conservative

interpolation of the conserved quantities from the old distorted Lagrangian mesh to the new rezoned one. After remap the Lagrangian computation can continue. Such approach allows to follow the motion of the fluid in the Lagrangian sense, while also allows to be used for above mentioned types of flows (as e.g. shear or vortex) for which pure Lagrangian approach would fail.

2.4 Model for laser plasma

The simulations of problems involving laser generated plasma often involve large scale expansion or compression regions, see the expansion of a thin foil irradiated by a laser beam presented in Section 4.1 where the initial computational domain (a thin foil) volume grows more than 500 times. Thus for modeling of laser plasma one typically uses Lagrangian formulation presented in Section 2.2. The system (2) describes pure hydrodynamics and its energy equation has to be amended by terms describing two processes essential for laser plasma: heat conductivity and laser absorption. The full system with energy equation transformed into non-conservative equation for internal energy reads

$$\begin{aligned} \frac{1}{\rho} \frac{d\rho}{dt} + \operatorname{div} \mathbf{u} &= 0, \\ \rho \frac{d\mathbf{u}}{dt} + \operatorname{grad} p &= 0, \\ \rho \frac{d\varepsilon}{dt} + p \operatorname{div} \mathbf{u} &= \operatorname{div}(\kappa \operatorname{grad} T) - \operatorname{div} \mathbf{I}, \end{aligned} \tag{3}$$

where $T = T(\rho, \varepsilon)$ is the temperature, κ the heat conductivity, \mathbf{I} the laser energy flux density (Poynting vector). This system is the basic model which we employ for laser plasma simulations.

3 Numerical methods

3.1 Composite schemes for Euler formulation

There exist many difference schemes treating Euler equations in Euler formulation on static computational mesh [50, 24]. Comparison of several best known schemes, including e.g. PPM and WENO, on 1D and 2D test problems can be found in [36]. Here we deal with composite schemes, which we have developed in [32, 33].

3.1.1 1D schemes

In 1D the system of Euler equations is written as

$$U_t + f_x(U) = 0$$

where U is vector of conservative variables and f is the vector of fluxes of these variables. One of the simplest finite difference schemes for conservation laws is the Lax-Friedrichs (LF) scheme. Its two step version uses the predictor

$$U_{i+1/2}^{n+1/2} = \frac{1}{2}[U_i^n + U_{i+1}^n] - \frac{\Delta t}{2\Delta x}[f(U_{i+1}^n) - f(U_i^n)], \tag{4}$$

to get the solution $U_{i+1/2}^{n+1/2}$ on the dual grid (obtained from the primary grid by shifting both indexes i and n by $1/2$) from the solution U_i^n on the primary grid. The LF scheme is completed by the corrector

$$U_i^n = \frac{1}{2}[U_{i+1/2}^{n+1/2} + U_{i-1/2}^{n+1/2}] - \frac{\Delta t}{2\Delta x}[f(U_{i+1/2}^{n+1/2}) - f(U_{i-1/2}^{n+1/2})], \quad (5)$$

which is the predictor (4) shifted by $1/2$ in both indexes i and n and which computes the solution on the primary grid from that on the dual grid. The LF scheme is first order accurate and very diffusive. The other well known scheme is Lax-Wendroff (LW) scheme, which in its two step form uses the LF predictor (4) followed by the corrector

$$U_i^{n+1} = U_i^n - \frac{\Delta t}{\Delta x}[f(U_{i+1/2}^{n+1/2}) - f(U_{i-1/2}^{n+1/2})]. \quad (6)$$

Thanks to the centering the LW scheme is second order accurate, however it produces dispersive oscillations behind discontinuities. The numerical LW oscillations can be filtered out by the diffusive LF scheme, which is a filter consistent with the differential equation. This idea leads to global composition of LW and LF schemes which we call composite scheme [32]. Denoting L_W the operator of the LW scheme defined by (4), (6) and L_F the operator of the LF scheme defined by (4), (5), the composite scheme is defined by the global composition of $k - 1$ operators L_W followed by one operator L_F , i.e. by the operator

$$S_k = L_F \circ L_W \circ \dots \circ L_W,$$

so that

$$U^{n+k} = S_k U^n.$$

This composite scheme is called the LWLFk scheme.

The numerical behavior of the LW, LF and composite schemes is demonstrated in Fig. 1 presenting numerical solution of a single shock wave propagating to the right. The LW scheme produces dispersive oscillations, while the diffusive LF scheme smears the discontinuity over many computational cells. Their combination in the LWLF4 scheme retains the steep shock resolution of LW while removing almost all its oscillations, keeping only a small overshoot on the shock wave.

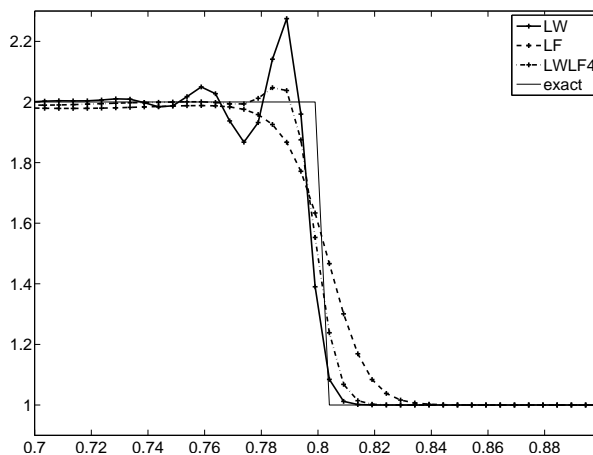


Figure 1: Density from a single shock wave computed by LW, LF and LWLF4 schemes.

3.1.2 2D schemes

In [33] we have proposed a new LF and LW type schemes in 2D. For the system (1) in 2D we define the predictor computing the solution on the dual grid from the solution on the primary grid (see Fig. 2 for primary and dual grids)

$$U_{i+1/2,j+1/2}^{n+1/2} = \frac{1}{4}[U_{i,j}^n + U_{i+1,j}^n + U_{i,j+1}^n + U_{i+1,j+1}^n] - \frac{\Delta t}{2\Delta x}[F_{i+1,j+1/2} - F_{i,j+1/2}] - \frac{\Delta t}{2\Delta y}[G_{i+1/2,j+1} - G_{i+1/2,j}], \quad (7)$$

where

$$F_{i+1,j+1/2} = \frac{1}{\Delta t \Delta y} \int_{y_j}^{y_{j+1}} \int_0^{\Delta t/2} f(\hat{U}(x_{i+1}, y, t)) dt dy,$$

and $\hat{U}(x_{i+1}, y, t)$ is the solution of the 1D Riemann problem (i.e. Cauchy initial problem

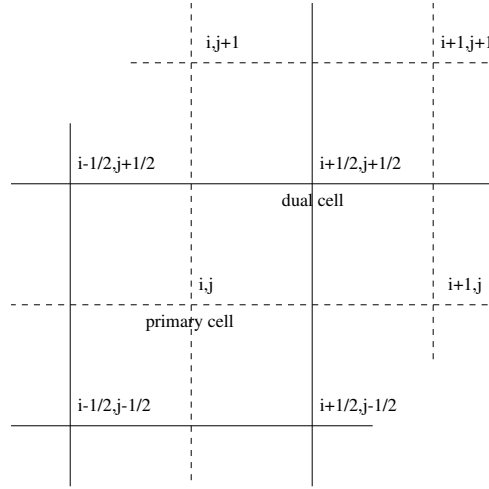


Figure 2: Staggered primary and dual grid in 2D, primary grid is shown as solid lines and dual grid as dashed lines

with initial conditions given by two constant states, one on the left of a given point and one on the right) with initial conditions

$$\hat{U}(x_{i+1}, y, 0) = \begin{cases} U_{i+1,j}^n & \text{for } y < y_{j+1/2} \\ U_{i+1,j+1}^n & \text{for } y > y_{j+1/2}. \end{cases}$$

In the same way

$$G_{i+1/2,j+1} = \frac{1}{\Delta t \Delta x} \int_{x_i}^{x_{i+1}} \int_0^{\Delta t/2} g(\hat{U}(x, y_{j+1}, t)) dt dx,$$

and $\hat{U}(x, y_{j+1}, t)$ is the solution of the Riemann problem with initial conditions

$$\hat{U}(x, y_{j+1}, 0) = \begin{cases} U_{i,j+1}^n & \text{for } x < x_{i+1/2} \\ U_{i+1,j+1}^n & \text{for } x > x_{i+1/2}. \end{cases}$$

The solutions of the Riemann problems is approximated by the 1D LF predictor giving the numerical fluxes

$$F_{i+1,j+1/2} = f \left(\frac{1}{2}[U_{i+1,j+1} + U_{i+1,j}] - \frac{\Delta t}{4\Delta y}[g(U_{i+1,j+1}) - g(U_{i+1,j})] \right), \quad (8)$$

and

$$G_{i+1/2,j+1} = g \left(\frac{1}{2} [U_{i+1,j+1} + U_{i,j+1}] - \frac{\Delta t}{4\Delta x} [f(U_{i+1,j+1}) - f(U_{i,j+1})] \right). \quad (9)$$

For scalar advection (i.e. (1) in 2D with $f(U) = aU, g(U) = bU$) the expanded predictor (7) has coefficients $(1 \pm \lambda)(1 \pm \mu)$ with $\lambda = a\Delta t/\Delta x, \mu = b\Delta t/\Delta y$. For $\max(|\lambda|, |\mu|) \leq 1$ the predictor is a positive scheme, thus it is stable. The 2D LF corrector is defined similarly like in 1D by shifting all indexes n, i, j by $1/2$ in the predictor formula (7). The two step LF scheme is (as the predictor) optimally stable for scalar advection, i.e. it is stable for $\max(|\lambda|, |\mu|) \leq 1$.

The analog of 1D LW, i.e. the second order accurate 2D predictor-corrector scheme, is defined by the predictor (7) and the corrector

$$\begin{aligned} U_{i,j}^{n+1} &= U_{i,j}^n \\ &- \frac{\Delta t}{2\Delta x} [f(U_{i+1/2,j+1/2}) + f(U_{i+1/2,j-1/2}) - f(U_{i-1/2,j+1/2}) - f(U_{i-1/2,j-1/2})] \\ &- \frac{\Delta t}{2\Delta y} [g(U_{i+1/2,j+1/2}) + g(U_{i-1/2,j+1/2}) - g(U_{i+1/2,j-1/2}) - g(U_{i-1/2,j-1/2})]. \end{aligned} \quad (10)$$

We call this second order method the corrected Lax-Friedrichs (CF) scheme. As in 1D the composite is

$$LF \circ CF \circ \dots \circ CF \quad (11)$$

and is called CFLFk, consisting of $k - 1$ applications of CF followed by one LF. For scalar advection the CF scheme is optimally stable [33] and also composites are optimally stable.

As the presented composite schemes use the LF sub-step, the composite schemes are only first order accurate, however their numerical error is much smaller than the error of pure LF. To overcome this problem we have experimented in [33] with replacing LF in the composite by component-wise WENO [15] (i.e. WENO without eigenvector decomposition), however for some problems such a composite scheme is noisier than CFLF composites. The composite schemes have been used also for the shallow water equations [35]. The main advantage of composite schemes is their simplicity.

3.1.3 3D schemes

The generalization [34, 33] of the 2D two-step LF and CF schemes gives the predictor

$$\begin{aligned} U_{i+\frac{1}{2},j+\frac{1}{2},k+\frac{1}{2}}^{n+\frac{1}{2}} &= \frac{1}{8} (U_{i,j,k}^n + U_{i+1,j,k}^n + U_{i,j+1,k}^n + U_{i,j,k+1}^n \\ &\quad + U_{i,j+1,k+1}^n + U_{i+1,j,k+1}^n + U_{i+1,j+1,k}^n + U_{i+1,j+1,k+1}^n) \\ &\quad - \frac{\Delta t}{2\Delta x} \left(f \left(U_{i+1,j+\frac{1}{2},k+\frac{1}{2}}^{n+\frac{1}{4}} \right) - f \left(U_{i,j+\frac{1}{2},k+\frac{1}{2}}^{n+\frac{1}{4}} \right) \right) \\ &\quad - \frac{\Delta t}{2\Delta y} \left(g \left(U_{i+\frac{1}{2},j+1,k+\frac{1}{2}}^{n+\frac{1}{4}} \right) - g \left(U_{i+\frac{1}{2},j,k+\frac{1}{2}}^{n+\frac{1}{4}} \right) \right) \\ &\quad - \frac{\Delta t}{2\Delta z} \left(h \left(U_{i+\frac{1}{2},j+\frac{1}{2},k+1}^{n+\frac{1}{4}} \right) - h \left(U_{i+\frac{1}{2},j+\frac{1}{2},k}^{n+\frac{1}{4}} \right) \right). \end{aligned} \quad (12)$$

The values at the center of all faces of the primary cell (having one integer index and two half shifted indexes) on time level $n + 1/4$ are computed using the analog of the 2D

predictor (7)

$$\begin{aligned}
U_{i,j+\frac{1}{2},k+\frac{1}{2}}^{n+\frac{1}{4}} &= \frac{1}{4} (U_{i,j,k}^n + U_{i,j+1,k}^n + U_{i,j,k+1}^n + U_{i,j+1,k+1}^n) \\
&\quad - \frac{\Delta t}{4 \Delta y} \left(g \left(U_{i,j+1,k+\frac{1}{2}}^{n+C} \right) - g \left(U_{i,j,k+\frac{1}{2}}^{n+C} \right) \right) \\
&\quad - \frac{\Delta t}{4 \Delta z} \left(h \left(U_{i,j+\frac{1}{2},k+1}^{n+C} \right) - h \left(U_{i,j+\frac{1}{2},k}^{n+C} \right) \right),
\end{aligned} \tag{13}$$

with similar formulas for the other faces. The values at the center of the edges of the primary cell (having two integer indexes and one half shifted index) on time level $n + C$ are evaluated by an analog of 1D predictor (4):

$$U_{i+\frac{1}{2},j,k}^{n+C} = \frac{1}{2} (U_{i,j,k}^n + U_{i+1,j,k}^n) - C \frac{\Delta t}{\Delta x} (f(U_{i+1,j,k}^n) - f(U_{i,j,k}^n)), \tag{14}$$

with similar formulas for the other edges. Standard generalization of the 2D schemes to 3D leads to $C = 1/6$ and uses the values at the center of primary edges on time level $n + 1/6$, however later we will vary the value of C to stabilize the second order scheme. For scalar advection (i.e. (1) with $f(U) = aU, g(U) = bU, h(U) = cU$) the expanded predictor (12) (with $C = 1/6$) has coefficients $(1 \pm \lambda)(1 \pm \mu)(1 \pm \tau)$ with $\lambda = a\Delta t/\Delta x, \mu = b\Delta t/\Delta y, \tau = c\Delta t/\Delta z$. For $\max(|\lambda|, |\mu|, |\tau|) \leq 1$ the predictor is a positive scheme, thus it is stable. By the same procedure as in 1D and 2D, the LF corrector uses the same formulas with the indexes i, j, k and n shifted by a one half. The two step LF scheme is (as the predictor with $C = 1/6$) optimally stable for scalar advection, i.e. it is stable for $\max(|\lambda|, |\mu|, |\tau|) \leq 1$.

The CF (corrected Lax-Friedrichs) scheme uses the corrector

$$\begin{aligned}
U_{i,j,k}^{n+1} &= U_{i,j,k}^n - \frac{\Delta t}{\Delta x} \left(F_{i+\frac{1}{2},j,k} - F_{i-\frac{1}{2},j,k} \right) \\
&\quad - \frac{\Delta t}{\Delta y} \left(G_{i,j+\frac{1}{2},k} - G_{i,j-\frac{1}{2},k} \right) \\
&\quad - \frac{\Delta t}{\Delta z} \left(H_{i,j,k+\frac{1}{2}} - H_{i,j,k-\frac{1}{2}} \right),
\end{aligned} \tag{15}$$

where the fluxes at the centers of the edges of the primary cell are defined by simple averaging

$$\begin{aligned}
F_{i+\frac{1}{2},j,k} &= \frac{1}{4} \left(f \left(U_{i+\frac{1}{2},j+\frac{1}{2},k+\frac{1}{2}}^{n+\frac{1}{2}} \right) + f \left(U_{i+\frac{1}{2},j-\frac{1}{2},k+\frac{1}{2}}^{n+\frac{1}{2}} \right) \right. \\
&\quad \left. + f \left(U_{i+\frac{1}{2},j+\frac{1}{2},k-\frac{1}{2}}^{n+\frac{1}{2}} \right) + f \left(U_{i+\frac{1}{2},j-\frac{1}{2},k-\frac{1}{2}}^{n+\frac{1}{2}} \right) \right),
\end{aligned}$$

with similar formulas for the other edges.

The von Neumann stability analysis of the CF scheme with $C = 1/6$ for scalar advection uses the Fourier transformation $u_{ijk} = \bar{u} e^{i(\alpha + j\beta + k\gamma)}$. The package FIDE [26] of the computer algebra system Reduce [11] evaluated the amplification factor of the scheme as

$$|f|^2 = 1 + 4A \frac{\lambda\mu\tau \tan(\alpha/2) \tan(\beta/2) \tan(\gamma/2) D + AB}{D^2}$$

where

$$\begin{aligned}
A &= \lambda \tan(\alpha/2) + \mu \tan(\beta/2) + \tau \tan(\gamma/2) \\
B &= \sum_{j=0}^1 \sum_{k=0}^1 \sum_{m=0}^1 \tan^{2j}(\alpha/2) \tan^{2k}(\beta/2) \tan^{2m}(\gamma/2) (\lambda^{2j} \mu^{2k} \tau^{2m} - 1) \\
D &= (\tan(\alpha/2)^2 + 1)(\tan(\beta/2)^2 + 1)(\tan(\gamma/2)^2 + 1)
\end{aligned}$$

The von Neumann stability condition of the scheme is $\forall \alpha \forall \beta \forall \gamma |f| \leq 1$. This formula is too complicated to be analyzed algebraically. However the analysis can be completed for a special case $\mu = \tau = \lambda, \gamma = \pi/2$ for which the amplification factor is

$$|f|^2 = 1 + \frac{f_n}{(\tan(\alpha/2)^2 + 1)^2 (\tan(\beta/2)^2 + 1)^2}$$

where

$$\begin{aligned}
f_n &= [((t_a^2 t_b^2 + t_a^2 + t_b^2 + \lambda^2 t_a^2 t_b^2) \lambda^4 - (2t_a^2 t_b^2 + 2t_a^2 + 2t_b^2 + 1))(t_a + t_b + 1) \\
&\quad + (2t_a^3 t_b^3 + 2t_a^3 t_b + t_a^3 + t_a^2 t_b + t_a^2 + 2t_a t_b^3 + t_a t_b^2 + 2t_a t_b + t_a + t_b^3 \\
&\quad + t_b^2 + t_b + 1) \lambda^2] (t_a + t_b + 1) \lambda^2 \\
t_a &= \tan(\alpha/2) \\
t_b &= \tan(\beta/2)
\end{aligned}$$

The quantifier elimination¹ program QEPCAD [13] has proved that the logical formula

$$\forall t_a \forall t_b \quad f_n \leq 0$$

is equivalent to the formula $\lambda = 0$. This shows that for the special case $\tau = \mu = \lambda \neq 0$ and $\gamma = \pi/2$ the absolute value of the amplification factor is greater than one and so the scheme is unstable. Numerical sampling of the amplification factor has shown that it is unstable for all non-zero values of λ, μ, τ . Note that also in [25] some 3D discretizations are unconditionally unstable.

The composite schemes CFLFk in 3D are constructed as in 2D (11) and consist of $k - 1$ CF steps and one LF step. The composite schemes are sub-optimally stable [33].

The modified equation approach revealed that the instability of CF (with the predictor (12)-(14) with $C = 1/6$ and the corrector (15)) is caused by terms $U_{xyz}, U_{xyyz}, U_{xyzz}$ in

¹The quantifier elimination (QE) is the procedure which transforms the formula

$$Q_1 x_1 \in R, Q_2 x_2 \in R, \dots, Q_k x_k \in R, \quad F(x_1, \dots, x_m),$$

where $m \geq k$, $Q_i, i = 1, \dots, k$ are quantifiers either \forall (for all) or \exists (there exists) and F is an arbitrary logical combination of polynomial equations or inequalities in the real variables x_1, \dots, x_m , into the equivalent formula which does not contain any quantifier and contains only non-quantified variables x_{k+1}, \dots, x_m and is again a logical combination of polynomial equations and inequalities. In [48] Tarski has proved that QE is possible and in [49] he gave the algorithm for doing QE, however, the complexity of the algorithm was prohibitive. In [7] Collins presented a new method for QE by the cylindrical algebraic decomposition (CAD) with double exponential complexity. Based on this Hong [13] developed the program QEPCAD (Quantifier Elimination by Partial Cylindrical Algebraic Decomposition) which incorporates many important improvements of the original CAD algorithm. We have developed a methodology for using QE for stability analysis [14], which includes not only the stability of difference schemes, but also stability of ordinary differential equations, well-posed analysis of partial differential equations and stability of boundary conditions and their numerical approximations.

the modified equation computed by the FIDE [26] package. These terms come from the flux terms of the form $f(g(h(u)))$ (with arbitrary ordered f, g, h). This has lead us to variations of the constant C . The predictor with $C = 0$ has for scalar advection the coefficients $(1 \pm \lambda)(1 \pm \mu)(1 \pm \tau) \pm \lambda\mu\tau$, which do not include the term $\lambda\mu\tau$ which is related to stability. With $C = 0$ the amplification factor of the CF scheme is

$$|F_{CF}|^2 = 1 + 4 \frac{(\lambda t_a + \mu t_b + \tau t_c)^2}{(1 + t_a^2)^2 (1 + t_b^2)^2 (1 + t_c^2)^2} [(\lambda t_a \mu t_b + \lambda t_a \tau t_c + \mu t_b \tau t_c)^2 + \lambda^2 t_a^2 + \mu^2 t_b^2 + \tau^2 t_c^2 - (1 + t_a^2)(1 + t_b^2)(1 + t_c^2) + 1],$$

where $t_a = \tan(\alpha/2), t_b = \tan(\beta/2), t_c = \tan(\gamma/2)$. This is again too complicated to be analyzed analytically. However for the special case $\lambda = \mu = \tau$ the von Neumann stability condition is equivalent to

$$\forall t_a, t_b, t_c \lambda^4 (t_a t_b + t_a t_c + t_b t_c)^2 + \lambda^2 (t_a^2 + t_b^2 + t_c^2) + 1 - (1 + t_a^2)(1 + t_b^2)(1 + t_c^2) \leq 0$$

and the quantifier elimination program QEPCAD [13] has proved that this is equivalent to $27\lambda^8 - 18\lambda^4 + 4\lambda^2 - 1 \leq 0$ [34]. The numerical sampling results in the stability region plotted in Fig. 3. We can conclude that the stability region includes the cube $\max(|\lambda|, |\mu|, |\tau|) < 0.8545$ where $\lambda = 0.8545$ is the only positive real root of the above polynomial.

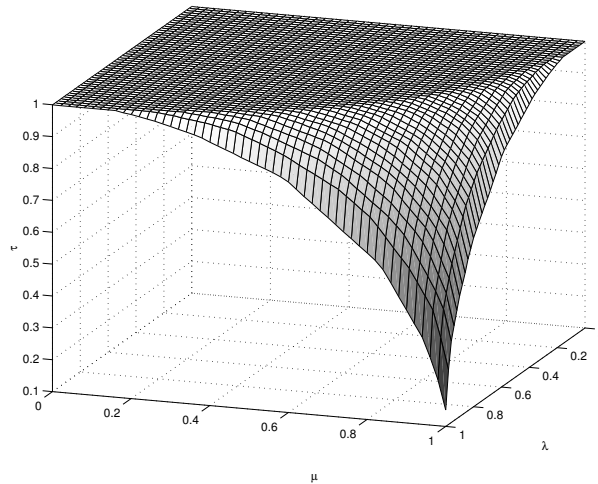


Figure 3: Stability region of 3D CF scheme with $C = 0$. Stability region is below the plotted surface in the λ, μ, τ space.

3.1.4 Optimally stable 3D schemes based on dimensional splitting

Here we will develop optimally stable, second order accurate scheme based on the 1D LW scheme and dimensional splitting [22]. The 1D LW scheme (4), (6) defines the 1D difference operator $U^{n+1} = L^x(U^n)$ in x (or corresponding index i) direction. In the same way we define the 1D operators L^y and L^z in y and z (or corresponding indexes j and k) directions. Now the simplest 3D non-symmetric dimensionally-split scheme is given by

$$U_{i,j,k}^{n+1} = L^x L^y L^z U_{i,j,k}^n.$$

This scheme is simple, fast and optimally stable, however it is not symmetric.

There are 6 different products of the operators L^x , L^y , and L^z in 3D, so to make a symmetric scheme, we average all these combinations:

$$U_{i,j,k}^{n+1} = \frac{1}{6}(L^x L^y L^z + L^x L^z L^y + L^y L^x L^z + L^y L^z L^x + L^z L^x L^y + L^z L^y L^x)(U_{i,j,k}^n). \quad (16)$$

This scheme is second-order accurate, symmetric and optimally stable, however it is a dimensionally split scheme and we would like to develop a non-split scheme. To get the conservation form

$$U_{i,j,k}^{n+1} = U_{i,j,k}^n - \frac{\Delta t}{\Delta x} \left(F_{i+\frac{1}{2},j,k}^{n+\frac{1}{2}} - F_{i-\frac{1}{2},j,k}^{n+\frac{1}{2}} \right) - \frac{\Delta t}{\Delta y} \left(G_{i,j+\frac{1}{2},k}^{n+\frac{1}{2}} - G_{i,j-\frac{1}{2},k}^{n+\frac{1}{2}} \right) - \frac{\Delta t}{\Delta z} \left(H_{i,j,k+\frac{1}{2}}^{n+\frac{1}{2}} - H_{i,j,k-\frac{1}{2}}^{n+\frac{1}{2}} \right). \quad (17)$$

of 3D scheme (16), we use linear transformations of the type $(f(A)+f(B))/2 \rightarrow f((A+B)/2)$ to collect all terms with the same flux at the same point, e.g. for the point $(n+\frac{1}{2}, i+\frac{1}{2}, j, k)$

we get $F_{i+\frac{1}{2},j,k}^{n+\frac{1}{2}}$:

$$\begin{aligned} f^{-1}(F_{i+\frac{1}{2},j,k}^{n+\frac{1}{2}}) &= \frac{1}{2}(U_{i+1,j,k}^n + U_{i,j,k}^n) \\ &- \frac{\Delta t}{6 \Delta z} (h_{i+1,j,k+\frac{1}{2}}^{n+\frac{1}{2}} - h_{i+1,j,k-\frac{1}{2}}^{n+\frac{1}{2}}) - \frac{\Delta t}{6 \Delta z} (h_{i,j,k+\frac{1}{2}}^{n+\frac{1}{2}} - h_{i,j,k-\frac{1}{2}}^{n+\frac{1}{2}}) \\ &- \frac{\Delta t}{6 \Delta y} (g_{i+1,j+\frac{1}{2},k}^{n+\frac{1}{2}} - g_{i+1,j-\frac{1}{2},k}^{n+\frac{1}{2}}) - \frac{\Delta t}{6 \Delta y} (g_{i,j+\frac{1}{2},k}^{n+\frac{1}{2}} - g_{i,j-\frac{1}{2},k}^{n+\frac{1}{2}}) \\ &- \frac{\Delta t}{12 \Delta z} (\hat{H}_{i+1,j,k+\frac{1}{2}}^{n+\frac{1}{2}} - \hat{H}_{i+1,j,k-\frac{1}{2}}^{n+\frac{1}{2}}) - \frac{\Delta t}{12 \Delta z} (\hat{H}_{i,j,k+\frac{1}{2}}^{n+\frac{1}{2}} - \hat{H}_{i,j,k-\frac{1}{2}}^{n+\frac{1}{2}}) \\ &- \frac{\Delta t}{12 \Delta y} (\hat{G}_{i+1,j+\frac{1}{2},k}^{n+\frac{1}{2}} - \hat{G}_{i+1,j-\frac{1}{2},k}^{n+\frac{1}{2}}) - \frac{\Delta t}{12 \Delta y} (\hat{G}_{i,j+\frac{1}{2},k}^{n+\frac{1}{2}} - \hat{G}_{i,j-\frac{1}{2},k}^{n+\frac{1}{2}}) \\ &- \frac{\Delta t}{2 \Delta x} (f[U_{i+1,j,k}^n \\ &\quad - \frac{\Delta t}{3 \Delta y} (g_{i+1,j+\frac{1}{2},k}^{n+\frac{1}{2}} - g_{i+1,j-\frac{1}{2},k}^{n+\frac{1}{2}}) - \frac{\Delta t}{3 \Delta z} (h_{i+1,j,k+\frac{1}{2}}^{n+\frac{1}{2}} - h_{i+1,j,k-\frac{1}{2}}^{n+\frac{1}{2}}) \\ &\quad - \frac{\Delta t}{6 \Delta z} (\hat{H}_{i+1,j,k+\frac{1}{2}}^{n+\frac{1}{2}} - \hat{H}_{i+1,j,k-\frac{1}{2}}^{n+\frac{1}{2}}) - \frac{\Delta t}{6 \Delta y} (\hat{G}_{i+1,j+\frac{1}{2},k}^{n+\frac{1}{2}} - \hat{G}_{i+1,j-\frac{1}{2},k}^{n+\frac{1}{2}})] \\ &- f[U_{i,j,k}^n \\ &\quad - \frac{\Delta t}{3 \Delta y} (g_{i,j+\frac{1}{2},k}^{n+\frac{1}{2}} - g_{i,j-\frac{1}{2},k}^{n+\frac{1}{2}}) - \frac{\Delta t}{3 \Delta z} (h_{i,j,k+\frac{1}{2}}^{n+\frac{1}{2}} - h_{i,j,k-\frac{1}{2}}^{n+\frac{1}{2}}) \\ &\quad - \frac{\Delta t}{6 \Delta z} (\hat{H}_{i,j,k+\frac{1}{2}}^{n+\frac{1}{2}} - \hat{H}_{i,j,k-\frac{1}{2}}^{n+\frac{1}{2}}) - \frac{\Delta t}{6 \Delta y} (\hat{G}_{i,j+\frac{1}{2},k}^{n+\frac{1}{2}} - \hat{G}_{i,j-\frac{1}{2},k}^{n+\frac{1}{2}})]), \end{aligned} \quad (18)$$

where

$$\begin{aligned}
\hat{H}_{i,j,k+\frac{1}{2}}^{n+\frac{1}{2}} = h & \left(\frac{1}{2} (U_{i,j,k+1}^n + U_{i,j,k}^n) - \frac{\Delta t}{2 \Delta y} (g_{i,j+\frac{1}{2},k+1}^{n+\frac{1}{2}} - g_{i,j-\frac{1}{2},k+1}^{n+\frac{1}{2}}) \right. \\
& \quad \left. - \frac{\Delta t}{2 \Delta y} (g_{i,j+\frac{1}{2},k}^{n+\frac{1}{2}} - g_{i,j-\frac{1}{2},k}^{n+\frac{1}{2}}) \right. \\
& \quad \left. - \frac{\Delta t}{2 \Delta z} [h(U_{i,j,k+1}^n - \frac{\Delta t}{\Delta y} (g_{i,j+\frac{1}{2},k+1}^{n+\frac{1}{2}} - g_{i,j-\frac{1}{2},k+1}^{n+\frac{1}{2}})) \right. \\
& \quad \left. - h(U_{i,j,k}^n - \frac{\Delta t}{\Delta y} (g_{i,j+\frac{1}{2},k}^{n+\frac{1}{2}} - g_{i,j-\frac{1}{2},k}^{n+\frac{1}{2}}))] \right), \tag{19}
\end{aligned}$$

and in the same way

$$\begin{aligned}
\hat{G}_{i,j+\frac{1}{2},k}^{n+\frac{1}{2}} = g & \left(\frac{1}{2} (U_{i,j+1,k}^n + u_{i,j,k}^n) - \frac{\Delta t}{2 \Delta z} (h_{i,j+1,k+\frac{1}{2}}^{n+\frac{1}{2}} - h_{i,j+1,k-\frac{1}{2}}^{n+\frac{1}{2}}) \right. \\
& \quad \left. - \frac{\Delta t}{2 \Delta z} (h_{i,j,k+\frac{1}{2}}^{n+\frac{1}{2}} - h_{i,j,k-\frac{1}{2}}^{n+\frac{1}{2}}) \right. \\
& \quad \left. - \frac{\Delta t}{2 \Delta y} [g(U_{i+1,j,k}^n - \frac{\Delta t}{2 \Delta z} (h_{i,j+1,k+\frac{1}{2}}^{n+\frac{1}{2}} - h_{i,j+1,k-\frac{1}{2}}^{n+\frac{1}{2}})) \right. \\
& \quad \left. - g(U_{i,j,k}^n - \frac{\Delta t}{2 \Delta z} (h_{i,j,k+\frac{1}{2}}^{n+\frac{1}{2}} - h_{i,j,k-\frac{1}{2}}^{n+\frac{1}{2}}))] \right). \tag{20}
\end{aligned}$$

Here the fluxes $g_{i,j+1/2,k}^{n+1/2}$, $h_{i,j,k+1/2}^{n+1/2}$ are the flux values at predicted solutions $g_{i,j+1/2,k}^{n+1/2} = g(U_{i,j+1/2,k}^{n+1/2})$, $h_{i,j,k+1/2}^{n+1/2} = h(U_{i,j,k+1/2}^{n+1/2})$, where the predicted solutions $U_{i,j+1/2,k}^{n+1/2}$, $U_{i,j,k+1/2}^{n+1/2}$ are obtained by the analogs of 1D predictor (4) in y and z (or corresponding indexes j and k) directions.

Similar expressions for the other numerical fluxes $G_{i,j+1/2,k}^{n+1/2}$ and $H_{i,j,k+1/2}^{n+1/2}$ has been derived. The 3D dimensional splitting based scheme is then defined by (17). It is the non-split, symmetric, 2-nd order accurate and optimally stable scheme [22].

3.2 Indirect ALE method

We have developed the 2D ALE code PALE (Prague ALE) [27] for laser plasma simulations. Here we start to describe numerical methods used in this code for the hydrodynamics part, i.e. the left hand side of the equations, of the model (3) for laser plasma.

3.2.1 Lagrangian methods

The PALE code employs the staggered Lagrangian discretization method which defines kinematic variables (position and velocity) in mesh nodes and thermodynamic variables (density, internal energy, pressure, temperature) in the mesh cells. We use the logically orthogonal quadrilateral mesh. Each quadrilateral cell is divided into four quadrilateral sub-cells having vertexes in mesh nodes, centers of the cells and mid-points of the edges. Density is discretized also on the sub-cells. The staggered compatible method [4] uses forces acting on the mesh nodes which determine the nodes velocity. Basic force is the pressure force originating in pressure gradient. The sub-zonal pressure force [5] reflects the difference between cell and sub-cell pressures and is designed to prevent the hourglass mesh motion inverting quadrilateral cells. The last force is the artificial viscosity force (using either edge viscosity [6] or tensor viscosity [3]) which is adding necessary dissipation

to the shock waves to be able to numerically resolve them. The compatible method uses the internal energy equation from (3) which is not in conservative form. However the discretization is done in a compatible way which guarantees conservation of the total energy. Shortly each force performs work which is accounted in the appropriate internal energy update. The forces are acting from sub-cells surrounding the node to the node, while internal energy is discretized in cells, so the internal energy update in the cell includes the work of the forces from the four sub-cells which belong to the cell. To show that the method conserves the total energy, one needs to rearrange the sum over the nodes (including the change of kinetic energy) into sum over cells (including the work done by the forces from four sub-cells).

For the Lagrangian stage of the indirect ALE method one can also use composite schemes [45, 30, 31] or cell centered methods [39, 38], which have attracted recently much attention.

3.2.2 Lagrangian mesh rezoning

Mesh rezoning is the process which improves the geometric quality of the distorted Lagrangian mesh without changing its connectivity. The geometric quality of the mesh is bad when some internal angles of its cells are either too small, i.e. close to zero, or too big, i.e. close to 180° or greater than 180° (internal angle of the cell can be greater than 180° for non-convex cells). The mesh resulting from the Lagrangian step can be of low quality, e.g. when Lagrangian mesh, moving with the fluid, is being stretched by shear or vortex flow, and smoothing process changes the mesh in a way to improve its quality. The Winslow smoothing method [53] is one of the simplest smoothing methods. For a logically rectangular mesh the new positions of the mesh nodes are computed (with a possible iteration over l starting at the Lagrangian mesh) by

$$\mathbf{X}_{i,j}^{l+1} = \frac{1}{2(\alpha^l + \gamma^l)} \left(\alpha^l (\mathbf{X}_{i,j+1}^l + \mathbf{X}_{i,j-1}^l) + \gamma^l (\mathbf{X}_{i+1,j}^l + \mathbf{X}_{i-1,j}^l) - \frac{1}{2} \beta^l (\mathbf{X}_{i+1,j+1}^l - \mathbf{X}_{i-1,j+1}^l + \mathbf{X}_{i-1,j-1}^l - \mathbf{X}_{i+1,j-1}^l) \right),$$

where the coefficients $\alpha^l = x_\xi^2 + y_\xi^2$, $\beta^l = x_\xi x_\eta + y_\xi y_\eta$, $\gamma^l = x_\eta^2 + y_\eta^2$, and (ξ, η) are logical coordinates $\xi_i = i/n_x$, $\eta_j = j/n_y$ for $i = 1, \dots, n_x$ and $j = 1, \dots, n_y$ for a mesh with $n_x \times n_y$ nodes. The derivatives x_ξ, x_η are approximated by the central differences $(x_\xi)_{i,j} \approx (x_{i+1,j} - x_{i-1,j})/(2 \Delta\xi)$, $(x_\eta)_{i,j} \approx (x_{i,j+1} - x_{i,j-1})/(2 \Delta\eta)$ and similarly for y .

Other smoothing methods include the condition number smoothing [18] or the Reference Jacobian Method [19]. Usually one requires that each node during the rezone does not move out of the set of all old cells having this node as their vertex. For logically rectangular mesh this guarantees that each new cell is included inside the 3×3 patch of the old cells (see Fig. 4) and the remapping process described in the next section can be local.

If the distorted Lagrangian mesh is tangled, i.e. some of its cells are inverted (the cell becomes inverted when during the movement of its nodes, some node crosses some edge of the cell), then one either needs to use untangling (see e.g. [51]) or go back one Lagrangian time step to situation when the Lagrangian mesh has not been tangled and smooth this mesh.

3.2.3 Remapping

After rezoning of the Lagrangian distorted mesh we have a new, smoother, better mesh, however the hydrodynamical quantities are defined on the old Lagrangian mesh. To use the new mesh we have to interpolate these quantities from the old to the new mesh. As we are dealing with conservation laws, we conservatively interpolate the conserved quantities. The conservative interpolation of the discrete conserved quantities from the old mesh to the new one is called remapping.

Typically the remapping stage is divided into two steps: reconstruction and integration. First, the remapped conservative quantity, e.g. density ρ , is reconstructed from the discrete values by a piecewise linear function on each old cell, e.g. with the Barth-Jespersen limiter [1]. The reconstructed density in the old cell c' is given by the linear function

$$\rho_{c'}(x, y) = \rho_{c'} + (\rho_x)_{c'}(x - x_{c'}) + (\rho_y)_{c'}(y - y_{c'}), \quad (21)$$

(where $(x_{c'}, y_{c'})$ is the centroid of the cell c'). The piecewise linear global reconstruction is given by

$$\rho_g(x, y) = \rho_{c'}(x, y) \text{ for } (x, y) \in c' \quad (22)$$

and the mass of the new cell \tilde{c} (a tilde accent denotes objects related to the new mesh) is

$$\tilde{m}_c = \int_{\tilde{c}} \rho_g(x, y) dV = \sum_{c' \in \mathcal{C}(c)} m_{\tilde{c}c'} = \sum_{c' \in \mathcal{C}(c)} \int_{I_{c'}^{\tilde{c}}} \rho_{c'}(x, y) dV, \quad (23)$$

where $m_{\tilde{c}c'}$ is the mass of the intersection $I_{c'}^{\tilde{c}} = \tilde{c} \cap c'$ of the new cell \tilde{c} with the old cell c' and $\mathcal{C}(c)$ is the set of all old cells neighboring the old cell c (both edge and corner neighbors, so that for the logically rectangular mesh the set $\mathcal{C}(c)$ includes the whole 3×3 patch of the old cells). An example of logically rectangular mesh, where the new cell $\tilde{c}_{i,j} = [\tilde{P}_{i,j}, \tilde{P}_{i+1,j}, \tilde{P}_{i+1,j+1}, \tilde{P}_{i,j+1}]$ intersects with all nine (3×3 patch) old cells $c_{k,l}, k = i - 1, i, i + 1, l = j - 1, j, j + 1$ is presented in Fig. 4(a). The mass $m_{\tilde{c}c'}$ of the intersection

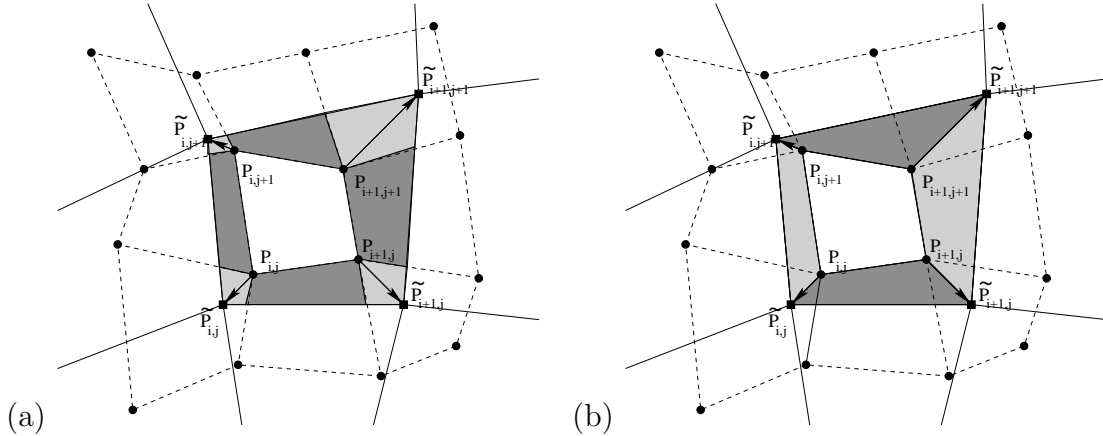


Figure 4: Old (dashed) and new (solid segments) mesh with intersection regions for the exact integration (a) and swept regions for the approximate integration (b).

$I_{c'}^{\tilde{c}}$ is now given by

$$\begin{aligned} m_{\tilde{c}c'} = \rho_{c'} \int_{I_{c'}^{\tilde{c}}} dV &+ (\rho_x)_{c'} \left(\int_{I_{c'}^{\tilde{c}}} x dV - x_{c'} \int_{I_{c'}^{\tilde{c}}} dV \right) \\ &+ (\rho_y)_{c'} \left(\int_{I_{c'}^{\tilde{c}}} y dV - y_{c'} \int_{I_{c'}^{\tilde{c}}} dV \right) \end{aligned} \quad (24)$$

where the integrals over the polygonal intersection are transformed using Green's theorem into integrals over the edges of the intersection and computed analytically. Now the remapped density on the new cell \tilde{c} is $\rho_{\tilde{c}} = \tilde{m}_c/V_{\tilde{c}}$, where $V_{\tilde{c}} = \int_{\tilde{c}} dV$ is the volume of the new cell \tilde{c} . This exact integration of reconstruction (22) is computationally rather expensive because it requires finding all cell intersections.

The approximate integration over swept regions [21], which are the regions swept by the cell edges moving from the old mesh to the new position in the new mesh (see Fig. 4 (b)), is much faster. The mass of the four swept regions has similar form as (24) with the intersection $I_{c'}^{\tilde{c}}$ replaced by the swept region.

The same remapping procedure is applied to the other conservative quantities, namely to density of momenta $\rho u, \rho v$ and total energy ρe . In both intersection and swept region method the masses (24) of intersections or swept regions can be interpreted as remap fluxes and the remapping formula can be written in a conservative flux form.

Even when the slopes in the reconstruction (21) are limited the remapping can introduce new local extrema (origin of numerical oscillations) into the remapped values. To remove such a new local extrema one can use a repair procedure [46, 37] which conservatively redistributes conserved quantities in such a way that the remapping does not introduce any new local extrema. The repair is a post-processing *ad hoc* correction. Better treatment, based on flux corrected transport (FCT) and called flux corrected remap, which guarantees that new local extrema are not introduced, is presented in the next section.

3.2.4 Flux corrected remapping of density

The flux corrected remapping [52] applies the idea of flux corrected transport [2, 54, 23, 43] to remapping. We assume that the continuous rezone strategy is employed, meaning that each new cell \tilde{c} is contained in the union of the old cells $c' \in \mathcal{C}(c)$. Based on this assumption we require that the value of the remapped density, $\tilde{\rho}_c$, has to be in the bounds given by density values on the old cells $c' \in \mathcal{C}(c)$

$$\rho_c^{\min} \leq \tilde{\rho}_c \leq \rho_c^{\max}, \quad \rho_c^{\min} = \min_{c' \in \mathcal{C}(c)} (\rho_{c'}), \quad \rho_c^{\max} = \max_{c' \in \mathcal{C}(c)} (\rho_{c'}). \quad (25)$$

The mass of the new cell \tilde{c} (23) can be written in the flux form (see e.g. [40])

$$\tilde{m}_c = m_c + \sum_{c' \in \mathcal{C}(c), c' \neq c} F_{c,c'}^m, \quad (26)$$

where

$$F_{c,c'}^m = -F_{c',c}^m, \quad (27)$$

are mass remapping fluxes.

We assume that we have two different set of fluxes. The low order fluxes $F_{c,c'}^{m,L}$ produce remapped density satisfying the bounds (25). The high order fluxes $F_{c,c'}^{m,H}$ produce remapped density which is more accurate in smooth regions, however might violate the bounds (25), typically around discontinuities. We construct the mass flux as a linear combination of the low order and high order fluxes

$$F_{c,c'}^m = F_{c,c'}^{m,L} + C_{c,c'}^m dF_{c,c'}^m, \quad dF_{c,c'}^m = -dF_{c',c}^m = F_{c,c'}^{m,H} - F_{c,c'}^{m,L}, \quad (28)$$

where

$$0 \leq C_{c,c'}^m = C_{c',c}^m \leq 1$$

are some coefficients to be constructed. The fluxes $dF_{c,c'}^m$ are called anti-diffusive fluxes. We want to find $C_{c,c'}^m$ such that resulting fluxes satisfy the bounds (25) and are as close as possible to high-order fluxes in some sense.

By (28) the equation (26) for new mass can be rewritten as

$$\tilde{m}_c = \tilde{m}_c^L + \sum_{c'} C_{c,c'}^m dF_{c,c'}^m, \quad \tilde{m}_c^L = m_c + \sum_{c'} F_{c,c'}^{m,L}. \quad (29)$$

From here further on, the summation over c' means summation over $c' \in \mathcal{C}(c), c' \neq c$ as in (26). Defining $m_c^{\min} = \rho_c^{\min} V_c, m_c^{\max} = \rho_c^{\max} V_c$ with V_c being the volume of the old cell c , the bounds (25) can be written as

$$m_c^{\min} - \tilde{m}_c^L \leq \sum_{c'} C_{c,c'}^m dF_{c,c'}^m \leq m_c^{\max} - \tilde{m}_c^L. \quad (30)$$

We have assumed that the low-order fluxes satisfy the bounds $m_c^{\min} - \tilde{m}_c^L \leq 0 \leq m_c^{\max} - \tilde{m}_c^L$ and thus the constraints (30) can always be satisfied by choosing all $C_{c,c'}^m = 0$. The differences in (30) are usually denoted by

$$Q_c^{m,\max} = m_c^{\max} - \tilde{m}_c^L \geq 0, \quad Q_c^{m,\min} = m_c^{\min} - \tilde{m}_c^L \leq 0.$$

We first consider the right-hand inequality in (30)

$$\sum_{c'} C_{c,c'}^m dF_{c,c'}^m \leq Q_c^{m,\max}. \quad (31)$$

The sum on the left-hand side of this inequality can be divided into two sums according to the sign of $dF_{c,c'}^m$ and bounded by the first sum, since the second one is negative:

$$\sum_{c'} C_{c,c'}^m dF_{c,c'}^m = \sum_{dF_{c,c'}^m > 0} C_{c,c'}^m dF_{c,c'}^m + \sum_{dF_{c,c'}^m < 0} C_{c,c'}^m dF_{c,c'}^m \leq \sum_{dF_{c,c'}^m > 0} C_{c,c'}^m dF_{c,c'}^m. \quad (32)$$

Clearly the inequality

$$\sum_{dF_{c,c'}^m > 0} C_{c,c'}^m dF_{c,c'}^m \leq Q_c^{m,\max} \quad (33)$$

implies (31). Now we define

$$P_c^{m,+} := \sum_{dF_{c,c'}^m > 0} dF_{c,c'}^m \geq 0 \quad (34)$$

and consider the special case $P_c^{m,+} = 0$. This means that the sums in (34) and (33) are empty as all anti-diffusive fluxes $dF_{c,c'}^m$ are non-positive $dF_{c,c'}^m \leq 0$ and the inequality (31) is satisfied as $C_{c,c'}^m \geq 0, dF_{c,c'}^m \leq 0$ and $Q_c^{m,\max} \geq 0$. Now assuming $P_c^{m,+} > 0$ we rewrite (33) as

$$\sum_{dF_{c,c'}^m > 0} C_{c,c'}^m dF_{c,c'}^m \leq D_c^{m,+} P_c^{m,+}, \quad (35)$$

where

$$D_c^{m,+} = Q_c^{m,\max} / P_c^{m,+}. \quad (36)$$

If we introduce the definition (34) of $P_c^{m,+}$ into (35) and move $D_c^{m,+}$ inside the sum we get

$$\sum_{dF_{c,c'}^m > 0} C_{c,c'}^m dF_{c,c'}^m \leq \sum_{dF_{c,c'}^m > 0} D_c^{m,+} dF_{c,c'}^m, \quad (37)$$

which is satisfied if

$$C_{c,c'}^m \leq D_c^{m,+} \quad \text{for each } c' \quad \text{for which } dF_{c,c'}^m > 0. \quad (38)$$

This is the final constraint on $C_{c,c'}^m$ for the interface of the cells c and c' coming from the upper density-mass bound in the cell c .

For the lower density-mass bound, i.e. for the left inequality in (30), we proceed in the same way. We define

$$P_c^{m,-} = \sum_{dF_{c,c'}^m < 0} dF_{c,c'}^m \leq 0. \quad (39)$$

For $P_c^{m,-} = 0$ the lower bound is satisfied and for $P_c^{m,-} < 0$ we define

$$D_c^{m,-} = Q_c^{m,\min} / P_c^{m,-}. \quad (40)$$

The final constraint on $C_{c,c'}^m$ for the interface of the cells c and c' coming from the density-mass lower bound in the cell c is

$$C_{c,c'}^m \leq D_c^{m,-} \quad \text{for each } c' \quad \text{for which } dF_{c,c'}^m < 0. \quad (41)$$

So for the coefficient $C_{c,c'}^m$ on the interface of the cells c and c' we activate either the constraint (38) or the constraint (41) depending on the sign of $dF_{c,c'}^m$. The activated constraint guarantees that the bounds (25) are satisfied in the cell c . However we need to satisfy these bounds also in the other cell c' sharing this interface. If $dF_{c,c'}^m > 0$, then $dF_{c',c}^m = -dF_{c,c'}^m < 0$ and the corresponding coefficient $C_{c',c}^m = C_{c,c'}^m$ has to satisfy the constraint (38) coming from the upper bound in the cell c and the constraint (41) coming from the lower bound in the cell c' :

$$C_{c,c'}^m \leq D_c^{m,+}, \quad C_{c,c'}^m \leq D_{c'}^{m,-}.$$

Now if we choose

$$C_{c,c'}^m = \min(D_c^{m,+}, D_{c'}^{m,-}, 1) \quad \text{for } dF_{c,c'}^m > 0, \quad (42)$$

and in the same way for $dF_{c,c'}^m < 0$

$$C_{c,c'}^m = \min(D_c^{m,-}, D_{c'}^{m,+}, 1) \quad \text{for } dF_{c,c'}^m < 0, \quad (43)$$

then the density bounds (25) are satisfied for both cells c and c' . This gives us a simple procedure to compute the coefficients $C_{c,c'}^m$ in the formulas (28) such that the density bounds (25) are satisfied, and the resulting mass fluxes are in general more accurate than the low-order fluxes.

3.2.5 Synchronized flux corrected remapping of density, momentum and energy

The other conservative quantities being remapped are momentum and total energy. The mass m_c , momentum $\boldsymbol{\mu}_c$ and total energy E_c of the old mesh cell c are given by $m_c = \int_c \rho dV$, $\boldsymbol{\mu}_c = \int_c \rho \mathbf{u} dV$, $E_c = \int_c \rho e dV$ and define the mean values of velocity and internal energy in the old mesh cell c as $\mathbf{u}_c = \boldsymbol{\mu}_c/m_c$, $\varepsilon_c = E_c/m_c - \mathbf{u}_c^2/2$. We write the remapping of momentum and energy in the flux form

$$\tilde{\boldsymbol{\mu}}_c = \boldsymbol{\mu}_c + \sum_{c' \in \mathcal{C}(c), c' \neq c} \mathbf{F}_{c,c'}^\mu, \quad \tilde{E}_c = E_c + \sum_{c' \in \mathcal{C}(c), c' \neq c} F_{c,c'}^E$$

and require that the remapped values preserve bounds in velocity and internal energy:

$$\mathbf{u}_c^{\min} \leq \tilde{\mathbf{u}}_c = \tilde{\boldsymbol{\mu}}_c/\tilde{m}_c \leq \mathbf{u}_c^{\max}, \quad \varepsilon_c^{\min} \leq \tilde{\varepsilon}_c = \tilde{E}_c/\tilde{m}_c - \tilde{\mathbf{u}}_c^2/2 \leq \varepsilon_c^{\max},$$

where

$$\begin{aligned} \mathbf{u}_c^{\min} &= \min_{c' \in \mathcal{C}(c)} \mathbf{u}_{c'}, & \varepsilon_c^{\min} &= \min_{c' \in \mathcal{C}(c)} \varepsilon_{c'}, \\ \mathbf{u}_c^{\max} &= \max_{c' \in \mathcal{C}(c)} \mathbf{u}_{c'}, & \varepsilon_c^{\max} &= \max_{c' \in \mathcal{C}(c)} (\max(\varepsilon_{c'}, \tilde{\varepsilon}_c^L)), \end{aligned}$$

and $\tilde{\varepsilon}_c^L = \tilde{E}_c^L/\tilde{m}_c^L - 1/2(\tilde{\boldsymbol{\mu}}_c^L/\tilde{m}_c^L)^2$ is the low order internal energy with $\tilde{m}_c^L, \tilde{\boldsymbol{\mu}}_c^L, \tilde{E}_c^L$ computed with low order fluxes. The low order internal energy has to be included in the upper internal energy bound to guarantee that the low order approximation stays in bounds.

As with density we assume that we have low order momentum and energy fluxes $\mathbf{F}_{c,c'}^{\mu,L}, F_{c,c'}^{E,L}$ satisfying the bounds and more accurate high order fluxes $\mathbf{F}_{c,c'}^{\mu,H}, F_{c,c'}^{E,H}$. We construct the flux corrected fluxes as linear combination of the low order and high order fluxes:

$$\begin{aligned} \mathbf{F}_{c,c'}^\mu &= \mathbf{F}_{c,c'}^{\mu,L} + C_{c,c'}^\mu d\mathbf{F}_{c,c'}^\mu, & d\mathbf{F}_{c,c'}^\mu &= -d\mathbf{F}_{c',c}^\mu = \mathbf{F}_{c,c'}^{\mu,H} - \mathbf{F}_{c,c'}^{\mu,L}, \\ F_{c,c'}^E &= F_{c,c'}^{E,L} + C_{c,c'}^E dF_{c,c'}^E, & dF_{c,c'}^E &= -dF_{c',c}^E = F_{c,c'}^{E,H} - F_{c,c'}^{E,L}, \end{aligned}$$

where

$$0 \leq C_{c,c'}^\mu = C_{c',c}^\mu \leq 1, \quad 0 \leq C_{c,c'}^E = C_{c',c}^E \leq 1,$$

are some coefficients to be constructed. Note, that to keep the direction of velocity, the momentum limiter coefficient $C_{c,c'}^\mu$ remains scalar.

Let us first look at simultaneous remapping of density and momentum satisfying the bounds in density and velocity. The density limiter coefficient $C_{c,c'}^m$ has to satisfy constraints derived in the previous section from density bounds. When the remapped values of mass and momentum are substituted into the velocity bounds one obtains inequalities which depend linearly on the limiter coefficients $C_{c,c'}^m$ and $C_{c,c'}^\mu$. An extension of the derivation performed in the previous section for the density results in the constraints

$$\begin{aligned} C_{c,c'}^\mu d\mathbf{F}_{c,c'}^\mu - \mathbf{u}_c^{\max} C_{c,c'}^m dF_{c,c'}^m &\leq \frac{Q_c^{\mu,\max}}{P_c^{\mu,\max,+}} \max(\boldsymbol{\Psi}_{c,c'}^{c,\mu,\max}, \mathbf{0}), \\ C_{c,c'}^\mu d\mathbf{F}_{c,c'}^\mu - \mathbf{u}_c^{\min} C_{c,c'}^m dF_{c,c'}^m &\geq \frac{Q_c^{\mu,\min}}{P_c^{\mu,\min,-}} \min(\boldsymbol{\Psi}_{c,c'}^{c,\mu,\min}, \mathbf{0}). \end{aligned}$$

where

$$\begin{aligned}
\mathbf{Q}_c^{\mu,\max} &= \mathbf{u}_c^{\max} \tilde{m}_c^L - \tilde{\mu}_c^L \geq \mathbf{0}, \\
\mathbf{Q}_c^{\mu,\min} &= \mathbf{u}_c^{\min} \tilde{m}_c^L - \tilde{\mu}_c^L \leq \mathbf{0}, \\
\Psi_{c,c'}^{c,\mu,\max} &= d\mathbf{F}_{c,c'}^\mu - \mathbf{u}_c^{\max} dF_{c,c'}^m, \\
\Psi_{c,c'}^{c,\mu,\min} &= d\mathbf{F}_{c,c'}^\mu - \mathbf{u}_c^{\min} dF_{c,c'}^m, \\
\mathbf{P}_c^{\mu,\max,+} &= \sum_{\Psi_{c,c'}^{c,\mu,\max} \otimes \mathbf{0}} \Psi_{c,c'}^{c,\mu,\max} \geq \mathbf{0}, \\
\mathbf{P}_c^{\mu,\min,-} &= \sum_{\Psi_{c,c'}^{c,\mu,\min} \otimes \mathbf{0}} \Psi_{c,c'}^{c,\mu,\min} \leq \mathbf{0},
\end{aligned}$$

and where the relation operators \otimes , \otimes , in the sums defining \mathbf{P}' s mean, that the ζ component of the sum (i.e. \mathbf{P}'_ζ) includes only c' for which corresponding component $(\Psi_{c,c'})_\zeta$ has given sign. All other vector vector operations and relations are performed component by component. These constraints are derived in [28] and guarantee that the velocity bounds are satisfied in the cell c . Similar constraints are derived for the cell c' . Together with the constraints (42) or (43) for $C_{c,c'}^m$, derived from the density bounds, all these linear constraints define a convex polygon in the $(C_{c,c'}^m, C_{c,c'}^\mu)$ plane which is an admissible set of all $(C_{c,c'}^m, C_{c,c'}^\mu)$ for which density and velocity bounds are satisfied. The optimal choice of the limiting coefficients $C_{c,c'}^m, C_{c,c'}^\mu$ from the admissible set is in [28] achieved by minimization of a function which tries to keep the solution close to the high order method.

Generalization of the outlined flux corrected remap strategy to the case of remapping density, momentum and energy with bounds in density, velocity and internal energy has been developed in [29]. The internal energy bounds result in non-linear constraints in the limiting coefficients $C_{c,c'}^m, C_{c,c'}^\mu, C_{c,c'}^E$ and the constrained minimization problem gives us the values of the limiting coefficients. Results of selected cyclic remapping numerical tests of the developed methods, together with comparison of the results with results of [43], are presented in [28, 29].

3.3 Heat conductivity

The parabolic part of the energy equation from the system (3) is treated separately by splitting from the hyperbolic part of the whole system (3). The spatial discretization of the heat conductivity term $\text{div}(\kappa \text{grad} T)$ is performed by the mimetic method developed in [44] for logically rectangular, quadrilateral meshes and generalized in [9] to unstructured triangular meshes.

The basic idea of the mimetic method is that the discrete operators of divergence and gradient should satisfy the discrete analogs of integral identities for divergence and gradient, namely the divergence Green formula and the Gauss theorem. The Gauss theorem can be restated in a way expressing that gradient is the adjoint operator of divergence in inner products of scalar and vector functions. The mimetic method discretizes the temperature inside each cell and the heat flux $\mathbf{w} = -\kappa \text{grad} T$ at the mid-points of each edge by its projection on the normal to the edge. This discretization of vector heat flux guarantees the continuity of normal flux through each edge. The discrete divergence is derived in a standard way from the discrete analog of the divergence Green formula on a computational cell. On the spaces of discrete scalar (temperature) and vector (heat

flux) functions (defined on the mesh), the discrete analogs of the inner products of scalar and vector functions (defined on the continuum computational domain) are defined. Now the discrete gradient is constructed as the adjoint (in the discrete inner products on the computational mesh) of the discrete divergence. Neumann boundary conditions are naturally included in the method through the inner products. Such discretization works well for distorted meshes appearing quite often in Lagrangian hydrodynamics and it allows discontinuous diffusion coefficient. Implicit temporal discretization allows to use the hydrodynamics time step also for the heat conductivity step. The scheme results in a linear system with a symmetric, positive definite matrix. The conjugate gradient method, preconditioned by the altered direction implicit method, is applied as an effective iterative solver for this system.

The classical Spitzer-Harm plasma heat conductivity [47] is employed. This heat conductivity is non-linear in temperature and can produce non-linear heat waves, which appear often in the laser plasma. To be able to resolve well the non-linear heat wave a non-linear transformation, which moves the non-linearity from the heat conductivity to the time derivative coefficient, is applied.

For laser plasma the computed heat fluxes are often physically unrealistic, too high. Such heat fluxes cannot be carried by available electrons carrying most of the heat energy. Direct decrease of the heat flux magnitude (where needed) leads to oscillations and checker board patterns in temperature, thus the heat flux limiting has to be performed differently. In the regions where the unlimited heat flux violates the physical limits the heat conductivity is decreased by the ratio of the unlimited flux magnitude and the heat flux limit. The heat equation is then solved again with the updated heat conductivity.

3.4 Laser absorption

Laser absorption in plasma is modeled by the term $\text{div } \mathbf{I}$ in the internal energy equation from the system (3). An important notion for the laser absorption is a critical density. The critical density defines the critical surface which is the isosurface of electron density being equal to the critical density. The laser can propagate only in the regions of plasma with electron density less than the critical density. Typically most of the laser energy is absorbed around the critical surface. Laser absorption on the critical surface assumes that laser propagates without damping and refraction till the critical surface where it is absorbed.

Ray tracing is a more complicated method for the laser absorption modeling. The laser beam is split into many laser rays carrying initially appropriate energy depending on the radius. Propagating of each ray is computed (traced) independently. Inside a cell through which the ray propagates it does not change direction and deposits a part of its energy into plasma internal energy by inverse bremsstrahlung. On the cell edge the ray refracts according to Snell law with refraction plane being orthogonal to the electron density gradient. A special case is a full reflection near the critical surface when the ray on the edge reflects back.

Laser beam has cylindrical symmetry and most simulated problems are cylindrically symmetric (here all problems except oblique incidence on a thin foil studied in section 4.1), so one has to include cylindrical $r - z$ geometry. All numerical methods, initially designed in Cartesian geometry, have been generalized into cylindrical geometry with a special boundary condition on the symmetry axis z .

4 Simulations of laser interaction with targets

In this section we present several selected simulations of laser interaction with different targets. The simulations correspond to the experiments performed at Prague Asterix Laser System PALS.

4.1 Oblique incidence on thin foil

The oblique incidence of a laser beam on a $0.8 \mu\text{m}$ thin Aluminum foil is reasonably simple and provides initial insight into laser interactions with matter. This simulation is an initial study to double foil targets which are used for investigation of plasma-wall interactions [42]. The third harmonics Gaussian laser pulse with wavelength 438 nm , energy 36 J , full width half maximum (FWHM) length 250 ps and focal spot radius $40 \mu\text{m}$ interacts with 30° oblique thin foil. The simulation starts at time $t = 0$ and the laser maximum is at time $t = 250 \text{ ps}$. It uses Cartesian geometry as it is not cylindrically symmetric. The density of the developing laser plasma at three times 150 , 200 and 250 ps is presented in Fig. 5 in a logarithmic scale with computational mesh and a magenta isolines of the critical surface. Laser beam is vertical and is coming from above with the beam axis on

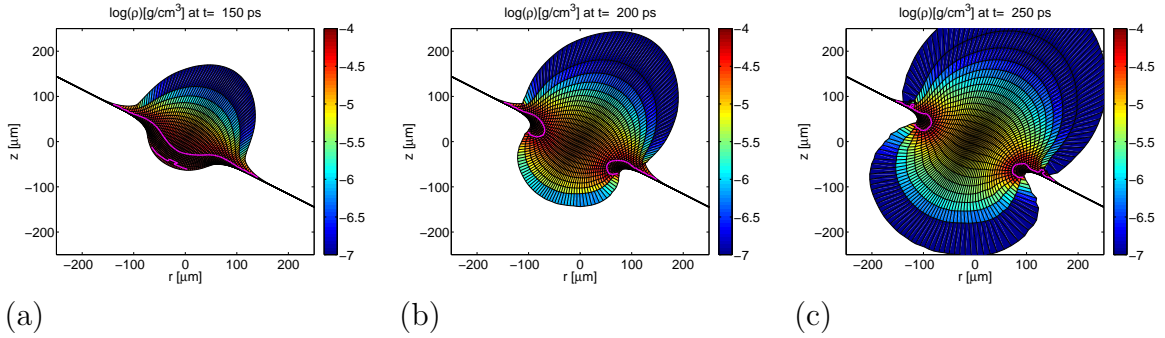


Figure 5: Density for interaction of oblique laser beam with a thin Aluminum foil at time: (a) 150 ps , (b) 200 ps and (c) 250 ps . Magenta curves denote the position of the critical surface.

the z axis $r = 0$. It propagates through the sub-critical plasma until the critical surface and is absorbed at the critical surface. In the beginning of the interaction laser energy is being deposited close to the upper boundary of the foil which starts to expand in the upper right direction creating plasma plume (corona). Before time 150 ps the whole foil in an area around the z axis is heated and secondary plume starts to expand in the lower left direction. At time 150 ps in Fig. 5 (a) the laser does not penetrate the foil, while at time 200 ps in Fig. 5 (b) the laser has already burned through the foil and only its small part, far from the z axis, is still being absorbed at the critical surface.

This simulation provides an example of a large scale change of computational domain (initial $0.8 \mu\text{m}$ thin foil expands to plumes of the size around $500 \mu\text{m}$ at Fig. 5 (c) at time of laser maximum, which is still not the end of the simulation), which dictates the use of Lagrangian coordinates moving with the moving plasma. Even when the laser is oblique to the foil, it heats the foil in such a way that the temperature and pressure gradients remain orthogonal to the foil. Pressure gradient drives the motion of plasma (3) and as it is orthogonal to the foil, also the expanding plasma plumes remain orthogonal to the foil.

4.2 Disc flyer target

The experimental setup of the disc flyer target, which has been used in experiments [8, 10] at PALS, is shown in Fig. 6. The Aluminum disc flyer of thickness d and radius r is located in the distance L from the Aluminum massive target and is parallel to the target surface. The disc flyer is irradiated by the intense laser pulse and ablatively accelerated towards massive target. The high velocity impact of the disc flyer on the massive target creates a crater in the massive target.

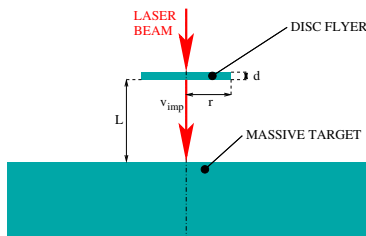


Figure 6: Experimental setup of disc flyer target.

The particular data of the simulated experiments [20] include: the disc radius $r = 150 \mu\text{m}$, the disc thickness $d = 6 \mu\text{m}$ or $d = 11 \mu\text{m}$ and the initial distance of the disc from target $L = 200 \mu\text{m}$. The disc is irradiated by laser pulse with energy $E = 120 \text{ J}$, 240 J or 390 J on the basic wavelength 1315 nm (1ω) and $E = 130 \text{ J}$ on the third harmonics with wavelength 438 nm (3ω). The radius of laser spot on target is $125 \mu\text{m}$ and the pulse duration (FWHM - full width half maximum) is 400 ps .

The simulation is split into two parts: ablative acceleration of the disc flyer and high velocity impact of the disc flyer on the massive target. The result of the first part, the accelerated disc flyer for $6 \mu\text{m}$ thick disc with 3ω 130 J laser pulse is presented in Fig. 7 showing the density and the computational mesh at time $t_{\text{imp}} = 1.1 \text{ ns}$, just before the disc flyer hits the massive target. The simulation starts at time $t = 0$ and the laser maximum is at time $t = 0.4 \text{ ns}$. The mass weighted averaged values of velocity in higher density

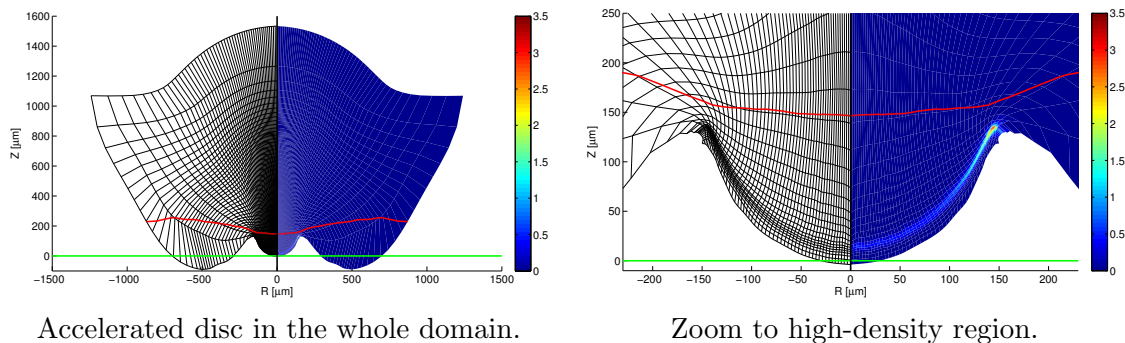


Figure 7: Density (in g/cm^3) and computational mesh of $6 \mu\text{m}$ thick disc accelerated disc by 3ω laser pulse of energy 130 J at time $t_{\text{imp}} = 1.1 \text{ ns}$. The green line denotes the massive target surface and the red curve is zero contour of the vertical z velocity component, i.e. the disc material below this curve is flying down towards the massive target while the material above this curve is moving up.

rectangular region for all simulated experiments at time of impact t_{imp} are compared in Table 1 with the measured experimental disc flyer velocities. The simulated disc flyer

velocities are generally somewhat higher than experimental ones with reasonably good agreement for $6\ \mu\text{m}$, 130 J, $3\ \omega$ and $11\ \mu\text{m}$, 120 J, $1\ \omega$ cases.

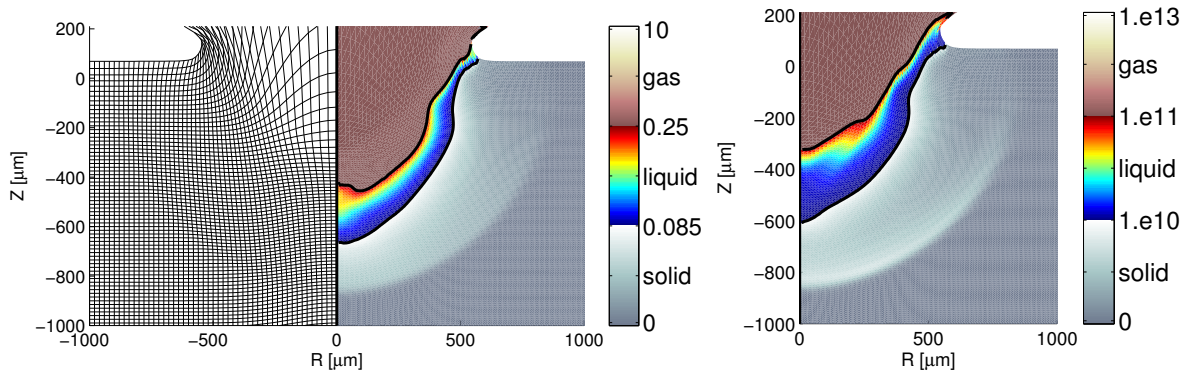
Problem	$t_{\text{imp}}[\text{ns}]$	$v_{\text{imp}}[\text{km/s}]$	$v_{\text{exp}}[\text{km/s}]$
$6\ \mu\text{m}$, 130 J, $1\ \omega$	2.2	88	60
$6\ \mu\text{m}$, 130 J, $3\ \omega$	1.1	153	150
$11\ \mu\text{m}$, 120 J, $1\ \omega$	3.4	46	40
$11\ \mu\text{m}$, 240 J, $1\ \omega$	2.4	76	54
$11\ \mu\text{m}$, 390 J, $1\ \omega$	2.0	104	?

Table 1: Time of impact t_{imp} , impact velocity from simulations v_{imp} , and experimental impact velocity v_{exp} . Symbol “?” denotes unavailable experimental velocity.

The initial data for the second part of the simulation, i.e. the high velocity impact, are obtained by remapping of the results of the first part (disc flyer acceleration) on the newly constructed mesh. The disc flyer in plasma state hits the massive target in high velocity, most of its kinetic energy is transformed into internal energy, which melts and evaporates target material creating the crater in the target. The impact creates approximately circular shock wave which propagates into the target and can be seen in Fig. 8 in solid material. The results at time $t = 80\ \text{ns}$ after the impact are presented in Fig. 8 in the form of temperature with computational mesh (a) and internal energy increase (b). The isolines distinguishing the phases in temperature are given by Aluminum melting and boiling points. The isolines distinguishing the phases in internal energy are given by specific heat needed to heat Aluminum to melting or boiling point together with heat of fusion and heat of vaporization needed for melting and evaporation of Aluminum. As the employed QEOS equation of state [41] is designed mainly for plasma and does not include heat of fusion and heat of vaporization the temperature and internal energy plots give different phase interfaces. By crater boundary we understand the liquid gas phase interface. The crater depth and radius estimated from temperature and internal energy simulation results are compared with the experimental data for all investigated cases in Table 2. For lower energies 120 J and 130 J the estimates from temperature correspond better to the experimental crater sizes while for higher energies 240 J and 390 J the internal energy estimates are closer to the experimental measurement. For the impact simulation we have to use the ALE method, as the pure Lagrangian simulation fails soon, e.g. for the $6\ \mu\text{m}$, 130 J, $3\ \omega$ case the Lagrangian computation fails around time $t = 0.5\ \text{ns}$.

Problem	experiment		temperature		energy	
	D_c	R_c	D_c	R_c	D_c	R_c
$6\ \mu\text{m}$, 130 J, $1\ \omega$	300	300	350	290	210	260
$6\ \mu\text{m}$, 130 J, $3\ \omega$	550	500	470	470	320	420
$11\ \mu\text{m}$, 120 J, $1\ \omega$	280	300	270	280	200	260
$11\ \mu\text{m}$, 240 J, $1\ \omega$	320	320	460	330	300	310
$11\ \mu\text{m}$, 390 J, $1\ \omega$	380	400	530	370	450	340

Table 2: Comparison of crater depth D_c and radius R_c (in μm) according to temperature and specific internal energy increase with experimental values.



(a) computational mesh and temperature (b) internal energy increase
 Figure 8: Computational mesh (only every second edge in each logical direction is visible) and temperature (in eV) (a) and specific internal energy increase (in erg/g) (b) of $6 \mu\text{m}$ thick disc irradiated by 130 J laser beam on third harmonic at time $t = 80 \text{ ns}$ after the impact. Solid, liquid and gas phases are separated by isolines in temperature and energy increase of melting and evaporation of Aluminum, different material phases are shown in different color maps.

4.3 Foam target

Foam layers are used in the ICF targets for smoothing different inhomogeneities appearing during laser target interactions. Simulations of laser interactions with foams are complicated by the difference between microscopic pore dimensions and macroscopic experimental scales. If the foam is modeled as a low density homogeneous material the laser is burning through the foam too fast, producing unrealistic results. This problem can be avoided by introducing structured model of the foam [16] shown in Fig. 9 (a) consisting from a series of parallel high-density slabs separated by low-density voids. When the laser burns through this structured model of foam it is delayed on each slab as it needs some time to burn through each slab. Here, we consider the interaction of the third

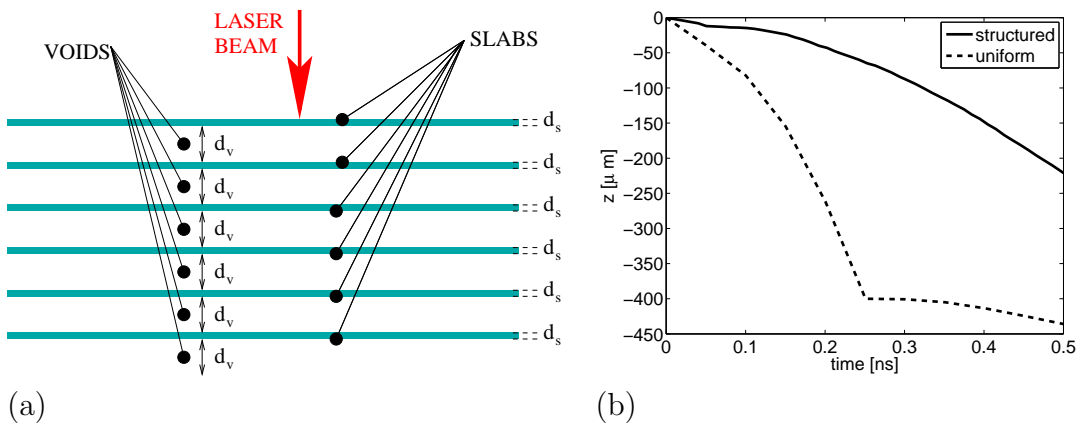


Figure 9: Structured model of the foam (a), burning of laser through the foam target (b).

harmonic Gaussian laser pulse of 320 ps FWHM duration, energy of 170 J and focal spot radius of $300 \mu\text{m}$ with $400 \mu\text{m}$ -thick layer of TAC foam of density 9.1 mg/cm^3 with $2 \mu\text{m}$ pores. Computation starts 500 ps before the laser maximum. The foam is modeled by uniform density 9.1 mg/cm^3 material and by structured model consisting from a sequence of $d_s = 0.018 \mu\text{m}$ thick dense slabs of density $\rho_s = 1 \text{ g/cm}^3$ separated by $d_v = 1.982 \mu\text{m}$

thick voids with density $\rho_v = 1 \text{ mg/cm}^3$ (giving the average density 9.1 mg/cm^3). The time evolution of the depth of the burned region of the foam on the z axis is plotted in Fig. 9 (b) for uniform and structured foam model with the initial upper surface of the foam at $z = 0$. The experimental speed of laser penetration into the foam before the laser pulse maximum (i.e. before time 0.5 ns) is about $600 \sim 700 \mu\text{m/ns}$, the speed from the structured simulation is about $500 \mu\text{m/ns}$ (average in time interval $(0.1, 0.5) \text{ ns}$) and from the uniform simulation about $1600 \mu\text{m/ns}$ (average in time interval $(0.0, 0.25) \text{ ns}$). The speed of burning through for the structured model is reasonably close to the experimental measurement, while this speed for the uniform model is more than twice higher.

4.4 Massive target irradiated by annular laser beam

In this section we investigate formation of plasma jets by interaction of annular laser beam with a massive Aluminum target. We use Gaussian in time laser pulse on 3-rd harmonics with FWHM length 400 ps and energy 10 J . The radial intensity profile of the annular beam is presented in Fig. 10(a). It has a 10% minimum on the z axis at $r = 0$, it is proportional to r^2 for small r and has a smooth maximum around $r = 600 \mu\text{m}$. Thanks to the annular radial laser profile the plasma plume develops and expands faster around the radial maximum of intensity at $r = 600 \mu\text{m}$, than around the z axis at $r = 0$. Such plume development leads to cone profile of higher density region visible in Fig. 10 (b) at 4 ns . The cone moves up in z direction and left in r direction towards the z axis and collides on the symmetry axis creating a plasma jet which can be seen in Fig. 11 (d) at 16 ns as high density, high pressure region along the z axis propagating up. Important is the radial pressure gradient on the cone directed inwards towards the z axis (which can be seen in Fig. 10 (c) showing the pressure at 4 ns) which drives the negative radial velocity towards the z axis, see the radial velocity plot at 4 ns in Fig. 10 (d).

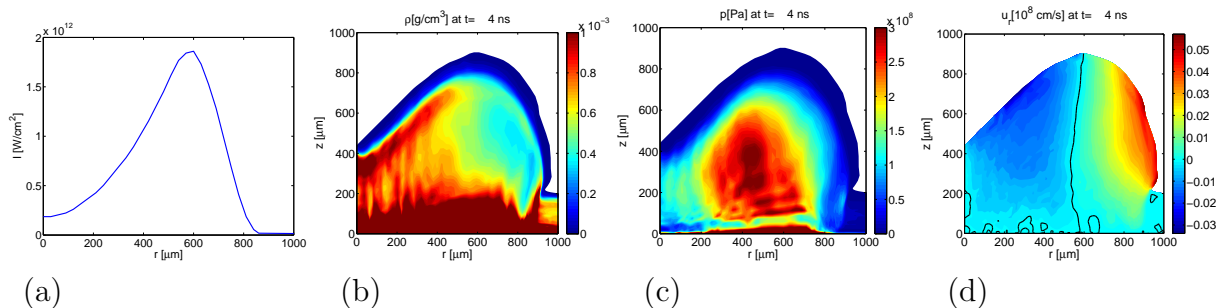


Figure 10: Plasma jet formation by annular laser beam: (a) radial laser intensity profile, (b) density, (b) pressure and (c) radial velocity distributions at time 4 ns .

The density evolution at times $2, 5, 8$ and 16 ns is presented in Fig. 11 (a),(b),(c),(d). The outlined dynamics of the plasma plume created by the annular laser provides a pure hydrodynamical mechanism for the plasma jets generation [17]. The plasma jets appear not only on the laser plasma micro-scale presented here, but also astrophysics deals with giant jets on the macro-scale.

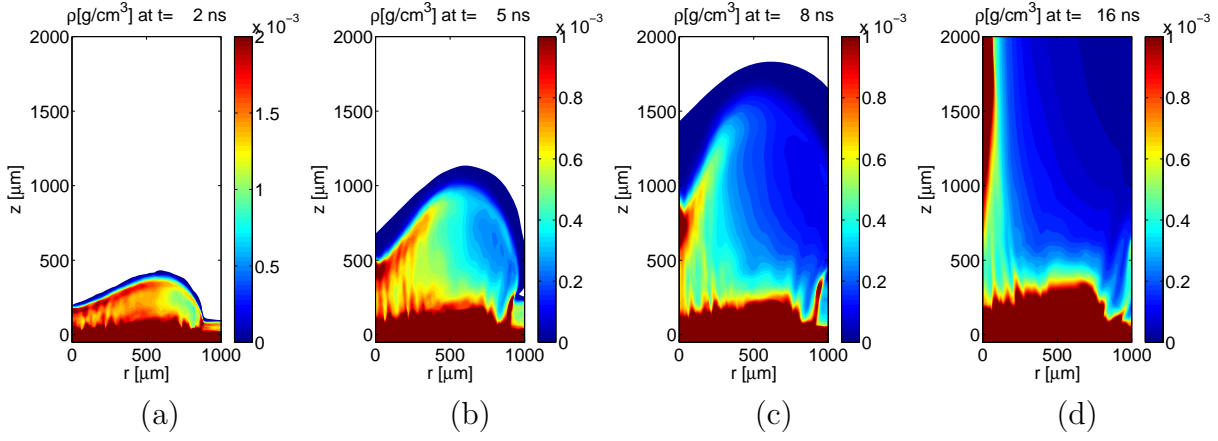


Figure 11: Plasma jet formation by annular laser beam: density evolution at times 2 (a), 5 (b), 8 (c) and 16 (d) ns; (d) pressure at 8 ns.

5 Outlook of the research and education in the given field

The field of numerical methods for compressible inviscid flow, called computational gas dynamics, belongs to a wider area of computational fluid dynamics, while at the same time spans over several traditional disciplines as aerospace engineering, mechanical engineering, meteorology, applied mathematics, numerical analysis, astrophysics or plasma physics. From the countless applications of gas dynamics we focus mainly on the fluid models of laser plasma. Further research in this field at the Faculty of Nuclear Sciences and Physical Engineering can concentrate on:

- improving existing Lagrangian methods, as e.g. developing new, better types of artificial viscosity,
- new numerical Lagrangian methods, as e.g. high order discrete Galerkin method,
- rezoning methods for grids with high aspect ratio cells,
- new remapping methods, as e.g. high order methods based on piecewise parabolic reconstruction,
- Lagrangian and ALE methods in 3D,
- improving the PALE code for laser plasma simulations by including models for another physical processes, as e.g. radiation transport or magnetic field.

The research is closely linked to the education at the Faculty of Nuclear Sciences and Physical Engineering. Supervised students work on the research project in the framework of their bachelor, master and Ph.D. theses. The advances in the research are reflected in the content of the courses for the study branch Computational Physics. The research can support the education in the following directions:

- new topics for the bachelor, master and Ph.D. theses,
- new courses reflecting the advances in computational gas dynamics,
- continue to incorporate students project into international cooperation.

References

- [1] T.J. Barth and D.C. Jespersen. The design and application of upwind schemes on unstructured meshes. Technical Report AIAA-89-0366, AIAA, NASA Ames Research Center, 1989.
- [2] J. Boris and D. Book. Flux-corrected transport I: SHASTA, a fluid transport algorithm that works. *J. Comput. Phys.*, 11:38–69, 1973.
- [3] J.C. Campbell and M.J. Shashkov. A tensor artificial viscosity using a mimetic finite difference algorithm. *J. Comput. Phys.*, 172(2):739–765, 2001.
- [4] E. J. Caramana, D. E. Burton, M. J. Shashkov, and P. P. Whalen. The construction of compatible hydrodynamics algorithms utilizing conservation of total energy. *J. Comput. Phys.*, 146(1):227–262, 1998.
- [5] E. J. Caramana and M. J. Shashkov. Elimination of artificial grid distortion and hourglass-type motions by means of Lagrangian subzonal masses and pressures. *J. Comput. Phys.*, 142:521–561, 1998.
- [6] E.J. Caramana, M. J. Shashkov, and P.P. Whalen. Formulations of artificial viscosity for multi-dimensional shock wave computations. *J. Comput. Phys.*, 144:70–97, 1998.
- [7] G. E. Collins. Quantifier elimination in the elementary theory of real closed fields by cylindrical algebraic decomposition. In *Lecture Notes in Computer Science*, pages 134–183, Berlin, 1975. Springer-Verlag. Vol. 33.
- [8] M. Kalal et.al. High power laser interaction with single and double layer targets. In *Proceedings of XXVIII ECLIM*, pages 249–259, Roma, September 6-10, 2004, 2005.
- [9] V. Ganzha, R. Liska, M. Shashkov, and C. Zenger. Mimetic finite difference methods for diffusion equations on unstructured triangular grid. In M. Feistauer, V. Dolejší, P. Knobloch, and K. Najzar, editors, *Numerical Mathematics and Advanced Applications ENUMATH 2003*, pages 368–377, Berlin, 2004. Springer-Verlag.
- [10] S. Yu. Guskov and et. al. Investigation of shock wave loading and crater creation by means of single and double targets in PALS-laser experiment. *J. of Russian Laser Research*, 26:228–244, 2005.
- [11] A. C. Hearn. REDUCE user’s manual, version 3.8. Technical report, Santa Monica, CA, 2004.
- [12] C.W. Hirt, A.A. Amsden, and J.L. Cook. An arbitrary Lagrangian-Eulerian computing method for all flow speeds. *J. Comput. Phys.*, 14:227–253, 1974. Reprinted in vol. 135(2), 203–216, 1997.
- [13] H. Hong. *Improvements in CAD-based Quantifier Elimination*. PhD thesis, The Ohio State University, 1990.
- [14] H. Hong, R. Liska, and S. Steinberg. Testing stability by quantifier elimination. *J. Symbolic Computation*, 24(2):161–187, 1997.
- [15] Guan-Shan Jiang and Chi-Wang Shu. Efficient implementation of weighted eno schemes. *J. Comp. Phys.*, 126:202–228, 1996.

- [16] T. Kapin, M. Kuchařík, J. Limpouch, and R. Liska. Hydrodynamic simulations of laser interactions with low-density foams. *Czechoslovak Journal of Physics*, 56:B493–B499, 2006.
- [17] V. Kmetík, J. Limpouch, R. Liska, and P. Váchal. Modeling of annular-laser-beam-driven plasma jets from massive planar targets. *Laser and Particle Beams*, 30(3):445–457, 2012.
- [18] P. Knupp. Achieving finite element mesh quality via optimization of the Jacobian matrix norm and associated quantities. Part I – a framework for surface mesh optimization. *Int. J. Numer. Meth. Eng.*, 48:401–420, 2000.
- [19] P. Knupp, L.G. Margolin, and M. Shashkov. Reference Jacobian optimization-based rezone strategies for arbitrary Lagrangian Eulerian methods. *J. Comput. Phys.*, 176:93–128, 2002.
- [20] M. Kuchařík, J. Limpouch, and R. Liska. Cylindrical 2D ALE simulations of laser interactions with flyer targets. *Czechoslovak Journal of Physics*, 56:B522–B527, 2006.
- [21] M. Kuchařík, M. Shashkov, and B. Wendroff. An efficient linearity-and-bound-preserving remapping method. *J. Comput. Phys.*, 188(2):462–471, 2003.
- [22] M. Kuchařík, R. Liska, S. Steinberg, and B. Wendroff. Optimally-stable second-order accurate difference schemes for nonlinear conservation laws in 3D. *Applied Numerical Mathematics*, 56(5):589–607, 2006.
- [23] D. Kuzmin, R. Löhner, and S. Turek, editors. *Flux-Corrected Transport. Principles, Algorithms and Applications*. Springer-Verlag, Berlin, 2005.
- [24] C.B. Laney. *Computational Gasdynamics*. Cambridge University Press, Cambridge, UK, 1998.
- [25] J.O. Langseth and R. J. LeVeque. A wave propagation method for three-dimensional hyperbolic conservation laws. *J. Comput. Phys.*, 165:126–166, 2000.
- [26] R. Liska and L. Drska. FIDE: A REDUCE package for automation of FInite difference method for solving pDE. In S. Watanabe and M. Nagata, editors, *ISSAC '90, Proceedings of the International Symposium on Symbolic and Algebraic Computation, Tokyo, August 20-24, 1990*, pages 169–176, New York, 1990. ACM Press, Addison Wesley.
- [27] R. Liska, M. Kuchařík, J. Limpouch, O. Renner, P. Váchal, L. Bednárik, and J. Velechovský. ALE method for simulations of laser-produced plasmas. In J. Fort, J. Furst, J. Halama, R. Herbin, and F. Hubert, editors, *Finite Volumes for Complex Applications VI, Problems & Perspectives*, volume 2, pages 57–73. Springer-Verlag, 2011.
- [28] R. Liska, M. Shashkov, P. Váchal, and B. Wendroff. Optimization-based synchronized flux-corrected conservative interpolation (remapping) of mass and momentum for arbitrary Lagrangian-Eulerian methods. *J. Comput. Phys.*, 229(5):1467–1497, 2010.
- [29] R. Liska, M. Shashkov, P. Váchal, and B. Wendroff. Synchronized flux corrected remapping for ALE methods. *Computers and Fluids*, 46:312–317, 2011.

- [30] R. Liska, M. Shashkov, and B. Wendroff. Lagrangian composite schemes on triangular unstructured grids. In M. Kočandrlová and V. Kellar, editors, *Mathematical and Computer Modelling in Science and Engineering*, pages 216–220, Prague, 2003.
- [31] R. Liska, M. Shashkov, and B. Wendroff. The early influence of Peter Lax on computational hydrodynamics and an application of Lax-Friedrichs and Lax-Wendroff on triangular grids in Lagrangian coordinates. *Acta Mathematica Scientia*, 31(6):2195–2202, 2011.
- [32] R. Liska and B. Wendroff. Analysis and computation with stratified fluid models. *J. Comput. Phys.*, 137:212–244, 1997.
- [33] R. Liska and B. Wendroff. Composite schemes for conservation laws. *SIAM J. Numer. Anal.*, 35(6):2250–2271, 1998.
- [34] R. Liska and B. Wendroff. Composite centered schemes for multidimensional conservation laws. In M. Fey and R. Jeltsch, editors, *Hyperbolic Problems: Theory, Numerics, Applications, Seventh International Conference in Zürich, February 1998, Vol. II*, pages 661–670, Basel, 1999. Birkhäuser, ISNM Vol.130.
- [35] R. Liska and B. Wendroff. Two-dimensional shallow water equations by composite schemes. *Int. J. Numer. Meth. Fluids*, 30:461–479, 1999.
- [36] R. Liska and B. Wendroff. Comparison of several difference schemes on 1D and 2D test problems for the Euler equations. *SIAM J. Scientific Computing*, 25(3):995–1017, 2003.
- [37] R. Loubère, M. Staley, and B. Wendroff. The repair paradigm: New algorithms and applications to compressible flow. *J. Comput. Phys.*, 211(2):385–404, 2006.
- [38] P-H. Maire. A high-order cell-centered Lagrangian scheme for two-dimensional compressible fluid flows on unstructured meshes. *J. Comput. Phys.*, 228(7):2391–2425, 2009.
- [39] P-H. Maire, R. Abgrall, J. Breil, and J. Ovadia. A cell-centered Lagrangian scheme for two-dimensional compressible flow problems. *SIAM Journal on Scientific Computing*, 29(4):1781–1824, 2007.
- [40] L.G. Margolin and M. Shashkov. Second-order sign-preserving conservative interpolation (remapping) on general grids. *J. Comput. Phys.*, 184:266–298, 2003.
- [41] R. M. More, K. Warren, D. Young, and G. Zimmerman. A new quotidian equation of state (qeos) for hot dense matter. *Phys. Fluids*, 31(10):3059–3078, 1988.
- [42] O. Renner, R. Liska, and F.B. Rosmej. Laser-produced plasma-wall interaction. *Laser and Particle Beams*, 27(4):725–731, 2009.
- [43] C. Schär and P.K. Smolarkiewicz. A synchronous and iterative flux-correction formalism for coupled transport equations. *J. Comput. Phys.*, 128:101–120, 1996.
- [44] M. Shashkov and S. Steinberg. Solving diffusion equation with rough coefficients in rough grids. *J. Comput. Phys.*, 129:383–405, 1996.

- [45] M. Shashkov and B. Wendroff. A composite scheme for gas dynamics in Lagrangian coordinates. *J. Comput. Phys.*, 150:502–517, 1999.
- [46] M. Shashkov and B. Wendroff. The repair paradigm and application to conservation laws. *J. Comput. Phys.*, 198(1):265–277, 2004.
- [47] L. Spitzer and R. Harm. Transport phenomena in a completely ionized gas. *Phys. Rev.*, 89:977–981, 1953.
- [48] A. Tarski. *The completeness of elementary algebra and geometry*. 1930. Reprinted in 1967.
- [49] A. Tarski. *A Decision Method for Elementary Algebra and Geometry*. Univ. of California Press, Berkeley, 1951. 2nd Ed.
- [50] E.F. Toro. *Riemann Solvers and Numerical Methods for Fluid Dynamics*. Springer-Verlag, Berlin, Heidelberg, 1997.
- [51] P. Váchal, R.V. Garimella, and M.J. Shashkov. Untangling of 2D meshes in ALE simulations. *J. Comput. Phys.*, 196(2):627–644, 2004.
- [52] P. Váchal and R. Liska. Sequential flux-corrected remapping for ALE methods. In A. Bermúdez de Castro, D. Gómez, P. Quintela, and P. Salgado, editors, *Numerical Mathematics and Advanced Applications. ENUMATH 2005*, pages 671–679. Springer Berlin Heidelberg New York, 2006.
- [53] A.M. Winslow. Equipotential zoning of two-dimensional meshes. Technical Report UCRL-7312, Lawrence Livermore National Laboratory, 1963.
- [54] S.T. Zalesak. Fully multidimensional flux-corrected transport algorithms for fluids. *J. Comput. Phys.*, 31:335–362, 1979.

Curriculum vitae

RICHARD LISKA

Address Czech Technical University in Prague
Faculty of Nuclear Sciences and Physical Engineering
Brehova 7, 115 19 Prague 1, Czech Republic

Phone +420-2 2435 8614

Fax +420-2 2435 8625

E-mail liska@siduri.fjfi.cvut.cz

Interests numerical treatment of conservation laws, Lagrangian and ALE methods for Euler equations, finite difference methods for partial differential equations, applied computer algebra, quantifier elimination, symbolic-numeric interfaces, laser plasma fluid simulations

Birthdate July 17, 1958

Education M.S. in Mathematical Engineering, Czech Technical University, 1982
Ph.D. in Mathematical-Physical Sciences, Czech Technical University, 1990

Positions Study stay, Czech Technical University, 1984-85
Ph.D. study, Czech Technical University, 1986-89
Research associate, Czech Technical University, 1989-1994
Researcher, Czech Technical University, 1994-1998
Associate professor, Czech Technical University, 1999-

Visiting positions Visiting associate professor, Teikyo University of Technology, Ichihara, Chiba, Japan, 6 months, 1992/11-1993/5
Visiting researcher, University of New Mexico, Albuquerque, USA, 1994-1999, 1 week - 1 month each year
Visiting researcher, Los Alamos National Laboratory, Los Alamos, USA, 1994-2011, 2 weeks - 2 months each year
Visiting researcher, CELIA, Université Bordeaux I, France, 1 month

Awards Price of Rector of Czech Technical University, 1988
Medal of minister of education for research results on composite schemes and their applications, 2001

Publications and citations 31 papers in impacted journals
Web of Science: 58 papers, 361 citations excluding auto-citations, H-index: 9
Selected publications: [14, 28, 29, 32, 33, 35, 36]

Education Teaching of courses *Differential equations on computer*, *Computer algebra*, *Practical engineering informatics 1*
Guarantor of bachelor and master program in *Computational Physics*
Vice chair of the committee of the Ph.D. program *Physical Engineering* for section *Computational Physics and Technics*
Supervisor of 4 bachelor theses, 15 master theses
Supervisor of 2 defended Ph.D. theses (Kuchařík, Váchal), supervising 2 Ph.D. students (Velechovský, Holec)